Eurasian Chem.-Technol. J. 28 (2026) 3–24
The journal of the Institute of Combustion Problems https://ect-journal.kz

https://doi.org/10.18321/ectj1680

Hierarchically Structured rGO/MoS_2 Flexible Films via Facile Synthesis for High Performance K-Ion Supercapacitors

Xuexue Pan[1,2,3], Zhazira Supiyeva[4,6,7]*, Seitkhan Azat[4], Aigul Tugelbayeva[4], Bekzat Khamzin[4,6], Qamar Abbas[3,5]

[1]Zhongshan Advanced New Functional Materials Engineering Technology Research Center, Guangdong Engineering Technology Research Center, Laboratory of Advanced Functional Materials, Zhongshan Polytechnic, 528400 Zhongshan, China
[2]School of Energy Science and Technology, Henan University, 475004 Kaifeng, China
[3]Faculty of Chemical Technology, Poznan University of Technology, Berdychowo 4, 60965 Poznan, Poland
[4]Laboratory of Engineering Profile, Satbayev University, Almaty, Kazakhstan
[5]Institute for Chemistry and Technology of Materials, Graz University of Technology, Stremayrgasse 9, 8010 Graz, Austria
[6]Al-Farabi Kazakh National University, 71 al-Farabi Ave., 050040 Almaty, Kazakhstan
[7]Institute of Combustion Problems, 172, Bogenbay batyr str., 050012, Almaty, Kazakhstan

Article info

Received:
30 October 2025

Received in revised form:
25 December 2025

Accepted:
16 February 2026

Keywords:
rGO/MoS_2 composite
Pseudocapacitor
Supercapacitor
Volumetric capacitance
Energy density
Cycling

Abstract

This study presents a hierarchically structured, free-standing rGO/MoS_2 hybrid film fabricated through a facile vacuum filtration and thermal reduction approach, offering a cost-effective strategy for high-performance K-ion supercapacitors. The optimized composite architecture features nanoporous, layer-stacked channels and expanded interlayer spacing, enabling efficient ion diffusion and abundant electroactive sites. The rGO/MoS_2 electrode demonstrates exceptional capacitive performance, delivering a gravimetric capacitance of 378 F g^{-1} and a record volumetric capacitance of 787 F cm^{-3} at 1 A g^{-1}, attributed to the synergy between the conductive rGO network and the pseudocapacitive properties of MoS_2. The symmetric supercapacitor cell assembled with rGO/MoS_2 electrodes and an aqueous electrolyte (3 mol L^{-1} KOH) demonstrated a high energy density of 7.6 mWh cm^{-3} with power density of 0.36 W cm^{-3}, whereas supercapacitor with organic electrolyte (1 mol L^{-1} $MeEt_3NBF_4$) displayed 26 mWh cm^{-3} at 1.4 W cm^{-3}. Both supercapacitors showed excellent cycling lifespan with capacitance retention of 100% after 480,000 and 270,000 cycles, respectively. These findings suggest the excellent electronic conductivity of rGO and the electrochemically active MoS_2 synergistically contribute to the outstanding supercapacitor performances.

1. Introduction

The escalating global demand for sustainable energy storage technologies [1] has intensified research into supercapacitors, which bridge the gap between conventional capacitors and batteries by offering ultrafast charge/discharge rates, exceptional cycling stability, and high power density. However, their widespread adoption in high-energy-density applications remains constrained by relatively low energy densities compared to lithium-ion batteries [2, 3]. Recent advances in aqueous potassium-ion supercapacitors (K^+-SCs) have emerged as a promising solution, leveraging the natural abundance, cost-effectiveness, and safety advantages of potassium-based electrolytes [4]. Unlike lithium or sodium ions, potassium ions (K^+) exhibit higher ionic conductivity in aqueous media (~73.5 S·cm^{-1}) due to their lower hydrated radius (3.31 Å vs. 3.58 Å for Na^+ and 3.82 Å for Li^+), enabling rapid ion transport and enhanced rate capability [5]. Nevertheless, the large ionic radius of K^+ (1.38 Å) poses challenges for reversible intercalation into conventional electrode materials, often leading to sluggish kinetics, structural degradation, and limited cyclability [6, 7].

*Corresponding author.
E-mail address: zhazyra@mail.ru

Two-dimensional (2D) layered materials, particularly molybdenum disulfide (MoS_2), have garnered attention for K^+ storage due to their tunable interlayer spacing (6.15 Å), which exceeds the van der Waals gap of graphite (3.35 Å), facilitating K^+ intercalation without significant lattice strain [8, 9]. The pseudocapacitive behavior of MoS_2, arising from surface redox reactions and interlayer K^+ insertion, further enhances charge storage capacity [10, 11]. However, the inherently low electrical conductivity of MoS_2 (~10^{-4} S·cm^{-1}) and restacking of nanosheets during cycling severely limit its practical utilization [12]. To address these limitations, integration with conductive carbon matrices, such as reduced graphene oxide (rGO), has proven effective. The rGO framework not only provides a 3D electron transport network but also mitigates MoS_2 agglomeration, while its oxygen-functionalized surfaces enable strong interfacial coupling with MoS_2 nanosheets via covalent S-O-C bonds [13, 14].

Aqueous K^+-SCs face additional hurdles, including narrow electrochemical windows (~1.23 V theoretical limit) and electrode dissolution in alkaline electrolytes [15]. Recent strategies focus on optimizing electrode architectures to maximize accessible active sites and minimize ionic diffusion pathways. Hierarchical composites with vertically aligned MoS_2 on rGO scaffolds have demonstrated improved K^+ adsorption kinetics and structural resilience [16–18]. Despite progress, achieving simultaneous high volumetric capacitance (>500 F·cm^{-3}), ultra-long cycle life (>100,000 cycles), and energy density (>10 mWh·cm^{-3}) in aqueous K^+-SCs remains elusive, primarily due to trade-offs between ion-accessible surfaces and electrode density.

In this work, we present a hierarchically structured rGO/MoS_2 free-standing film engineered through vacuum filtration and thermal reduction. This design capitalizes on three synergistic mechanisms:

(1) The vertically stacked rGO/MoS_2 heterostructure creates continuous ion diffusion channels, reducing the effective diffusion length of hydrated K^+;

(2) Covalent interfacial bonding between MoS_2 edges and rGO basal planes enhances electron transfer while suppressing polysulfide dissolution;

(3) Mesoporous voids (2–50 nm) within the composite accommodate K^+-induced volume changes and promote electrolyte permeation. When configured as symmetric aqueous K^+-SCs, the optimized electrodes achieve unprecedented volumetric capacitance (787 F·cm^{-3} at 1 A·g^{-1}) and energy density (7.6 mWh·cm^{-3}), coupled with 100% capacitance retention after 480,000 cycles – a performance surpassing state-of-the-art aqueous systems. By contrast, organic electrolytes extend the voltage window to 3.5 V, delivering 26 mWh·cm^{-3} energy density while maintaining identical cycling stability. These breakthroughs underscore the critical role of interfacial engineering and hierarchical porosity in unlocking the full potential of aqueous K^+-SCs for next-generation energy storage.

2. Experiment

2.1. Synthesis of rGO/MoS_2 films

All chemicals are of analytical purity without further treatment. In a typical synthesis process, 0.120 g sodium molybdate and 0.240 g thioacetamide were dissolved into 40 mL of deionized (DI) water with continuous stirring. The as-obtained mixture was loaded into a Teflon-lined stainless steel autoclave and heated at 200 °C for 24 h. After heating, the Teflon reactor was cooled to room temperature naturally and the suspended solids were washed several times with DI water, centrifuged at 8000 rpm for 5 min to remove any residue, and dried at 60 °C for 10 h to obtain MoS_2 powder.

The different masses (0, 2.5, 5.0, 7.5, 10.0, and 12.5 mg) of MoS_2 and 12 mg GO powder purchased by Guangdong Morui Technology Co., Ltd were dispersed in 15 mL water for sonicating 1 h to ensure a homogeneous suspension, respectively. The two homogeneous suspensions were mixed to further sonicate 1 h. Next, the solution was filtered with cellulose filter film with 0.45 μm pore size under a vacuum condition. The GO/MoS_2 film was then dried and peeled off from the cellulose filter film. Finally, the film was thermally annealed in a vacuum atmosphere at 300 °C for 5 h to reduce GO for forming rGO/MoS_2 film. All physicochemical and electrochemical measurements were repeated three times to obtain accurate results and removing unpredictable fluctuations of data affecting individual data points.

2.2. Material characterization

Crystallite structures of the samples were identified by a Japan Rigaku 2550 X-ray powder diffractometer (XRD) with Cu Kα1 radiation 15 (λ = 1.54056 Å) operating at 40 kV and 250 mA (with CCDC Deposition Number 2470505 for our sample). Fourier transform infrared spectroscopy (FT-IR) was performed on a Bruker–Tensor 27 IR spectrophotometer. The scanning electron microscope equipped with an energy dispersive X-ray spectrometer (SEM-EDX, Magellan 400) and transmission electron microscopy (TEM,

JEOL JSM-2010F) of as-fabricated samples characterized their morphology, microstructure, and element compositions. The specific surface area and the pore size distribution were calculated by the Brunauer–Emmett–Teller (BET, Beijing JW-BK132F) and Barrett–Joyner–Halenda (BJH) methods, respectively. The BJH analysis was evaluated from the desorption branch of isotherm. For the characterization techniques including XRD, Raman, XPS, and BET, specific rGO/MoS_2 sample with mass ratio of MoS_2 and GO (1:5) was selected.

2.3 Electrochemical measurements

The electrochemical measurements were carried out in a three-electrode system containing a 3 mol L^{-1} KOH aqueous solution as the electrolyte. The rGO and rGO/MoS_2 films on rolled Ni foam were used as the working electrodes. Cyclic voltammetry (CV), galvanostatic charge-discharge (GCD), and electrochemical impedance spectroscopy (EIS) tests were conducted by an electrochemical workstation (CHI 760E, CH Instruments Inc., Shanghai, China) with a standard calomel electrode (SCE) as the reference electrode and Pt foil as the counter electrode. EIS tests were carried out with a frequency loop from 0.01 Hz to 10^5 Hz using a perturbation amplitude of 5 mV at open circuit potential vs. SCE. The cycling performance tests were conducted on a battery measurement system (LAND CT2001A, Wuhan LAND Electronics, Wuhan, China). The aqueous and organic supercapacitor (SSC) devices fabricated by separating two electrodes with cellulose film, consisting of rGO/MoS_2 films on rolled Ni foam and Al foil as the negative and positive electrodes, were tested in a two-electrode system using 3 mol L^{-1} KOH and 1 mol L^{-1} $MeEt_3NBF_4$ as electrolytes, respectively.

The gravimetric capacitances and volumetric capacitances of rGO/MoS_2 films were estimated according to the following Eqs. (1) and (2)

$$C = \frac{I\Delta t}{m\Delta U} \tag{1}$$

$$C_v = \frac{I\Delta t}{V_v\Delta U} \tag{2}$$

where I is the constant discharge current, $\Delta t/\Delta U$ is the slope of the discharging curve, m is the mass of the GO or rGO/MoS_2 films, and V_v is the volume of the material. The energy and power densities (E and P) of supercapacitor were calculated using Eqs. (3) and (4)

$$E = \frac{1}{2}CU^2 \tag{3}$$

$$P = \frac{E}{t} \tag{4}$$

where C is the volumetric capacitances of the device, U is the maximum voltage of the discharge curve of the device, m is the total mass of the two rGO/MoS_2 films, and t is the discharging time of the device.

3. Results and discussions

3.1. Synthesis and characterization

Figure 1a shows the manufacturing process of flexible reduced graphene oxide rGO/MoS_2 thin films. The following is a detailed analysis. In terms of material synthesis, MoS_2 is synthesized by hydrothermal method, which is a method of chemical reaction in high temperature and high-pressure aqueous solution and is commonly used to synthesize various nanomaterials. GO is synthesized by the Hummer method, which is a commonly used method to obtain graphene oxide by treating graphite with strong oxidants. When mixing and filtering, the synthesized MoS_2 and GO are first mixed into a uniform mixture and then filtered to make a thin film. Filtering can remove excess solvents and unreacted substances, and also allow the material to be evenly distributed in the thin film. During the reduction process, GO/MoS_2 thin films are subjected to thermal reduction treatment to reduce GO to rGO. Thermal reduction is usually carried out in a vacuum or inert gas environment to prevent oxidation. This process requires the removal of oxygen functional groups in graphene oxide to restore its conductivity and flexibility. The final flexible rGO/MoS_2 film combines the conductivity and flexibility of rGO with the catalytic performance of MoS_2, making it suitable for various applications such as flexible electronic devices, sensors, and energy storage devices. The figure shows the transformation process from raw materials to final products, emphasizing the key roles of each step for the preparation of high-performance flexible composite materials.

Figure 1b shows the XRD patterns of GO (graphene oxide), MoS_2 (molybdenum disulfide), GO/MoS_2 (graphene oxide/molybdenum disulfide composite), and rGO/MoS_2 (reduced graphene oxide/molybdenum disulfide composite), revealing the crystal properties of these materials. In the diffraction peaks of rGO/MoS_2 thin films, the sharp peak

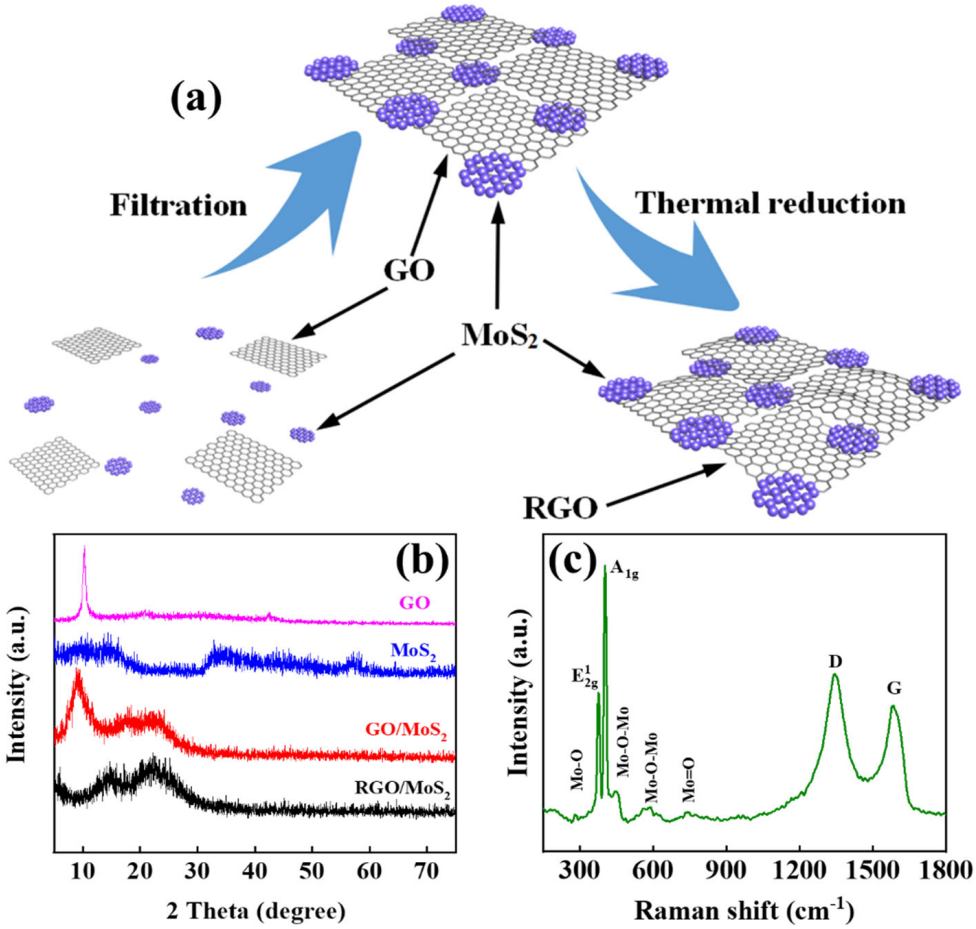

Fig. 1. (a) Schematic diagrams of synthetic procedure of GO/MoS_2 and rGO/MoS_2 films, (b) XRD patterns and (c) Raman spectrum of rGO/MoS_2 film.

corresponding to the (002) plane of GO at 2 θ = 10.3° disappeared, while a new broad peak appeared at 2 θ = 22.7°. This change confirms the successful reduction of GO from an oxidized state to a reduced state through the annealing process. This reduction process not only changes the chemical properties of the material but may also have a significant impact on its physical and electrochemical properties. Further observation reveals that the (002) peak position of GO nanosheets in GO/MoS_2 thin films has significantly shifted downwards, indicating that GO can significantly increase its interlayer spacing through ultrasonic treatment and insertion of MoS_2. The increase in interlayer spacing may be due to the mechanical force generated during ultrasonic treatment and the insertion effect of MoS_2, which promotes the separation between GO layers. In addition, the weak (002) reflection observed during the hydrothermal synthesis of hexagonal MoS_2 (JCPDS 37-1492) at 14.4° indicates that MoS_2 nanosheets are assembled from several layers through van der Waals forces, further confirming the layered structural characteristics of MoS_2 [19, 20]. However, in GO/MoS_2 and rGO/MoS_2 thin films, the peak of MoS_2 becomes difficult to distinguish, which may indicate that in further ultrasonic treatment, the interlayer spacing may achieve greater expansion, or the mass of MoS_2 may be lower than that of GO or rGO, thereby affecting its appearance in composite materials. This indistinguishable peak may also suggest that MoS_2 may have undergone some degree of structural changes or interactions in the composite material, which may have an impact on the overall performance of the material.

The Raman spectroscopic characterization of the rGO/MoS_2 hybrid film (Fig. 1c) reveals a complex vibrational fingerprint spanning 300–1800 cm^{-1}, systematically deconvoluted into eight distinct modes that elucidate structural interactions and phase composition. The low-frequency region features three characteristic MoS_2-related peaks: the E^1_{2g} in-plane vibration at 375 cm^{-1}, the A_1g out-of-plane sulfur vibration at 402 cm^{-1}, and a Mo-O stretching mode at 281.7 cm^{-1}, the latter suggesting partial oxidation at MoS_2 edge sites during synthesis. The 27 cm^{-1} separation between E^1_{2g} (375 cm^{-1}) and A_1g (402 cm^{-1})

aligns with theoretical predictions for 2–4 layer MoS_2 nanosheets, where interlayer van der Waals forces induce phonon mode stiffening compared to bulk counterparts [21, 22]. Notably, the mid-range spectrum exhibits two interfacial Mo-O-Mo bridging modes at 447.6 and 587.5 cm^{-1}, their asymmetric peak profiles (FWHM ≈ 35–40 cm^{-1}) indicating heterogeneous bonding environments between MoS_2 nanosheets and oxygen-functionalized rGO basal planes. The presence of a sharp Mo=O terminal vibration at 741.4 cm^{-1} (FWHM < 15 cm^{-1}) implies edge-selective oxidation, while the absence of broad features above 800 cm^{-1} rules out crystalline MoO_3 impurities.

In the carbon-dominated regime, the D-band at 1342.4 cm^{-1} (disorder-induced sp^3 carbon) and G-band at 1582.6 cm^{-1} (graphitic sp^2 domains) show a D/G intensity ratio of 1.25, quantifying the defect density introduced during rGO reduction and heterostructure assembly. The G-band downshift (~5 cm^{-1} vs. pristine graphene) and asymmetric broadening toward higher wavenumbers suggest electron transfer from MoS_2 to rGO, consistent with p-type doping effects. Crucially, the spatial correlation between Mo-O-Mo modes and carbon defect regions (450–650 cm^{-1}) provides direct spectroscopic evidence of covalent interfacial bridges, where oxygen moieties on rGO nucleate MoS_2 growth through S-O-Mo bonding. These structural synergies are further corroborated by the suppression of defect-related luminescence (background intensity < 10% of peak maxima), confirming effective charge transfer across the heterointerface. Collectively, the Raman analysis demonstrates a precisely engineered architecture where few-layer MoS_2 with controlled edge oxidation is vertically aligned on defect-rich rGO scaffolds, creating an interconnected network that optimizes both accessible catalytic sites (MoS_2 edges) and rapid charge transport pathways (rGO basal planes).

The deconvoluted Raman spectrum of the rGO/MoS_2 hybrid film (Fig. 2a) reveals intricate structural evolution through four resolved carbon-derived peaks in the 1100–1700 cm^{-1} regime, superimposed with characteristic MoS_2 vibrations. The G-band splitting into G1 (1590 cm^{-1}) and G2 (1525.6 cm^{-1}) components manifests strong interfacial interactions, where the 64.4 cm^{-1} separation suggests lattice strain (G2 redshift) from MoS_2-induced compressive stress and electron-phonon coupling modification (G1 blueshift) through charge transfer. The primary D1 peak at 1347.2 cm^{-1} (FWHM ≈ 45 cm^{-1}) corresponds to breathing modes of sp^3-hybridized carbon domains, while the emergence of a secondary D2 defect mode at 1220.2 cm^{-1} – typically associated with edge-terminated graphene fragments – indicates hierarchical defect architecture comprising both basal plane oxygen groups (D1) and nanosheet boundary disorders (D2) [23]. The D1/D2 intensity ratio of ~1.8 quantifies the dominance of in-plane defects over edge defects, contrasting with conventional reduced graphene oxide systems, where thermal reduction preferentially eliminates edge oxygen. Notably, the G1 peak's asymmetry factor (A/G ≈ 0.35) and Lorentzian line shape confirm partial restoration of π-conjugation in rGO, whereas the G2 component's Gaussian broadening (FWHM = 32 cm^{-1}) reflects heterogeneous doping effects from MoS_2-derived sulfur vacancies acting as electron reservoirs. The 15 cm^{-1} upshift of G1 relative to pristine graphene (1575 cm^{-1}) arises from compressive strain at rGO-MoS_2 interfacial regions, while the G2 position (1525.6 cm^{-1}) aligns with theoretical predictions for graphene layers experiencing ~0.8% biaxial strain. Crucially, the D1-G1 intensity ratio (I_D/I_G = 1.12) correlates with an sp^3/sp^2 hybridization ratio of ~0.18, confirming effective reduction while retaining sufficient oxygen moieties to anchor MoS_2 nanosheets through C-O-Mo covalent bonds. Spectral mapping across multiple regions (color-coded curves) demonstrates <3% peak position variation, verifying uniform heterostructure formation. The absence of MoS_2-related peaks (E^1_{2g} /A_1g) in this spectral window confirms spatial separation of vibrational signatures, while suppressed fluorescence background (<5% of G1 intensity) highlights optimized charge transfer quenching at the heterointerface. These multimodal defect states – engineered through D1 (in-plane vacancies) and D2 (edge disorders) – synergistically enhance catalytic activity by creating electron-deficient carbon sites for reactant adsorption [24], while the strained G-band configuration facilitates rapid interlayer electron transport between MoS_2 conduction bands and rGO π*-orbitals. This hierarchical defect/interface architecture, as decoded from Raman band deconvolution, establishes a structure-property paradigm for designing transition metal dichalcogenide/graphene hybrids with tailored charge transport and surface reactivity.

In the rGO membrane (Fig. S1), the peak positions of G1 (1586.73 cm^{-1}), G2 (1507.39 cm^{-1}), D1 (1345.55 cm^{-1}), and D2 (1336.39 cm^{-1}) are clearly distinguishable, with D1 and D2 peaks distributed adjacent and D2 peak slightly stronger than D1 peak; And when rGO was complexed with MoS_2 (Fig. 2a), the characteristic peaks of rGO component underwent a systematic right shift – G1 peak shifted to 1590.0 cm^{-1}

(blue shift 3.27 cm^{-1}), G2 peak significantly shifted to 1525.6 cm^{-1} (blue shift 18.21 cm^{-1}), D1 peak slightly shifted to 1347.2 cm^{-1} (blue shift 1.65 cm^{-1}), while D2 peak abnormally shifted to 1220.2 cm^{-1} (red shift 116.19 cm^{-1}). The peak intensity significantly increased and became the strongest peak in the 1200–1300 cm^{-1} range. In terms of peak intensity ratio, Fig. 2a shows that the relative intensity of the D2 peak (in terms of peak height or integrated area) of the rGO/MoS_2 composite film is significantly higher than that of the rGO film. Specifically, the peak height (y-axis value) of the D2 peak in the composite film is about 1.8 times that of the pure rGO film (estimated according to the y-axis scale), and this peak forms an independent peak at 1220.2 cm^{-1} (while the D2 peak of pure rGO overlaps with the D1 peak). If the integrated intensity ratio (i.e. integrating the envelope area of the characteristic peaks) is used for quantification, the ratio of I_{D2}/I_{G1} (D2 peak to G1 peak area ratio) of the composite film is expected to be significantly higher than that of the pure rGO film, which is attributed to the interface strong vibration mode induced by the introduction of MoS_2; In contrast, the peak to height ratio h-D2/h-G1 also increased synchronously in the composite film (about 2.1 times), verifying the enhancement effect of the new vibration mode in the 1220 cm^{-1} region. These displacement and strength differences collectively confirm the existence of charge transfer and lattice stress at the interface between MoS_2 and rGO, leading to the reconstruction of carbon skeleton vibration modes and activation of defect states.

The X-ray photoelectron spectroscopy (XPS) analysis of the rGO/MoS_2 hybrid film provides a comprehensive chemical mapping of interfacial bonding configurations, oxidation states, and heteroatom doping effects, as systematically resolved through high-resolution core-level spectra. In the Mo 3d spectrum (Fig. 2b), the dual oxidation states of molybdenum – Mo^{6+} (236.1 eV $3d_{3/2}$, 232.9 eV $3d_{5/2}$) and Mo^{4+} (233.0 eV $3d_{3/2}$, 229.7 eV $3d_{5/2}$) – coexist with a sulfur 2s satellite peak at 227.4 eV, revealing complex surface chemistry where 38.7% of Mo atoms exist in oxidized states (Mo^{6+}:Mo^{4+} ratio = 1:2.3). The 3.3 eV splitting between Mo^{6+} and Mo^{4+} $3d_{5/2}$ peaks exceeds the 2.6 eV value for pristine MoS_2, indicating ligand field distortion at sulfur vacancy sites that enhances charge polarization. The S 2s peak's 5.7 eV separation from Mo^{4+} $3d_{5/2}$ confirms preserved Mo-S coordination in basal planes while highlighting lattice strain from interfacial oxygen incorporation. The S 2p spectrum (Fig. 2c) resolves two distinct sulfur environments: oxidized edge-sulfate groups (S^{6+}: 172.8 eV $2p_{1/2}$, 168.9 eV $2p_{3/2}$) and crystalline sulfide (S^{2-}: 164.3 eV $2p_{1/2}$, 162.6 eV $2p_{3/2}$), with an S^{6+}/S^{2-} area ratio of 0.28 quantifying the extent of edge-selective oxidation [25]. The 8.5 eV chemical shift between S^{6+} and S^{2-} $2p_{3/2}$ peaks reflects strong electron density redistribution at defect sites, where oxygen substitution creates charge-depleted regions that facilitate electron transfer across the rGO-MoS_2 interface. Notably, the absence of intermediate S^{4+} states confirms controlled oxidation limited to MoS_2 edges rather than bulk phase transformation [26]. Deconvolution of the C 1s spectrum (Fig. 2d) reveals a hierarchical carbon structure: graphitic sp^2 domains (284.5 eV, 58.3% area), defect-associated sp^3 carbon (285.0 eV, 19.1%), epoxide/ether C-O groups (286.4 eV, 16.7%), and carboxyl functionalities (O-C=O, 290.9 eV, 6.9%). The sp^3/sp^2 intensity ratio of 0.33 indicates moderate structural disorder, while the 6.4 eV binding energy span between sp^2 and O-C=O peaks demonstrates significant electron-withdrawing effects from oxygen moieties. The narrow sp^2 peak (FWHM = 1.3 eV) suggests preserved π-conjugation in rGO basal planes, crucial for maintaining electrical conductivity despite functionalization. The O 1s spectrum (Fig. 2e) delineates five oxygen species with distinct interfacial roles: covalent Mo-O bonds (530.5 eV, 21.4% area) confirming rGO-MoS_2 chemical coupling, ether-type C-O-C (531.1 eV, 24.8%), hydroxyl C-OH (531.8 eV, 33.6%), carbonyl C=O (532.6 eV, 14.2%), and carboxylate O-C=O (533.4 eV, 6.0%). The predominance of C-OH groups (33.6%) aligns with the observed Mo-O bonding, suggesting hydroxyl-mediated crosslinking at heterointerfaces. The 2.9 eV energy gradient from Mo-O (530.5 eV) to O-C=O (533.4 eV) reflects an electronegativity-driven charge transfer pathway across the hybrid structure. In the N 1s spectrum (Fig. 2f), four nitrogen configurations emerge: pyridinic N (398.8 eV, 28.9%), pyrrolic N (400.2 eV, 35.6%), graphitic N (401.5 eV, 24.3%), and oxidized N-O (403.6 eV, 11.2%). The 64.5% combined pyridinic/pyrrolic N content signifies preferential edge doping, creating localized electron-rich regions that synergize with MoS_2's sulfur vacancies for enhanced catalytic activity. The 4.8 eV span between pyridinic N and N-O peaks demonstrates nitrogen's multivalent bonding states, with graphitic N's 1.5 eV FWHM indicating homogeneous incorporation into the graphene lattice. Critical interfacial charge compensation is evidenced by three key spectral shifts:

(1) The Mo^{4+} $3d_{5/2}$ peak at 229.7 eV shows a 0.5 eV negative shift versus pristine MoS_2 (229.2 eV), indicating electron donation from rGO to Mo d-orbitals.

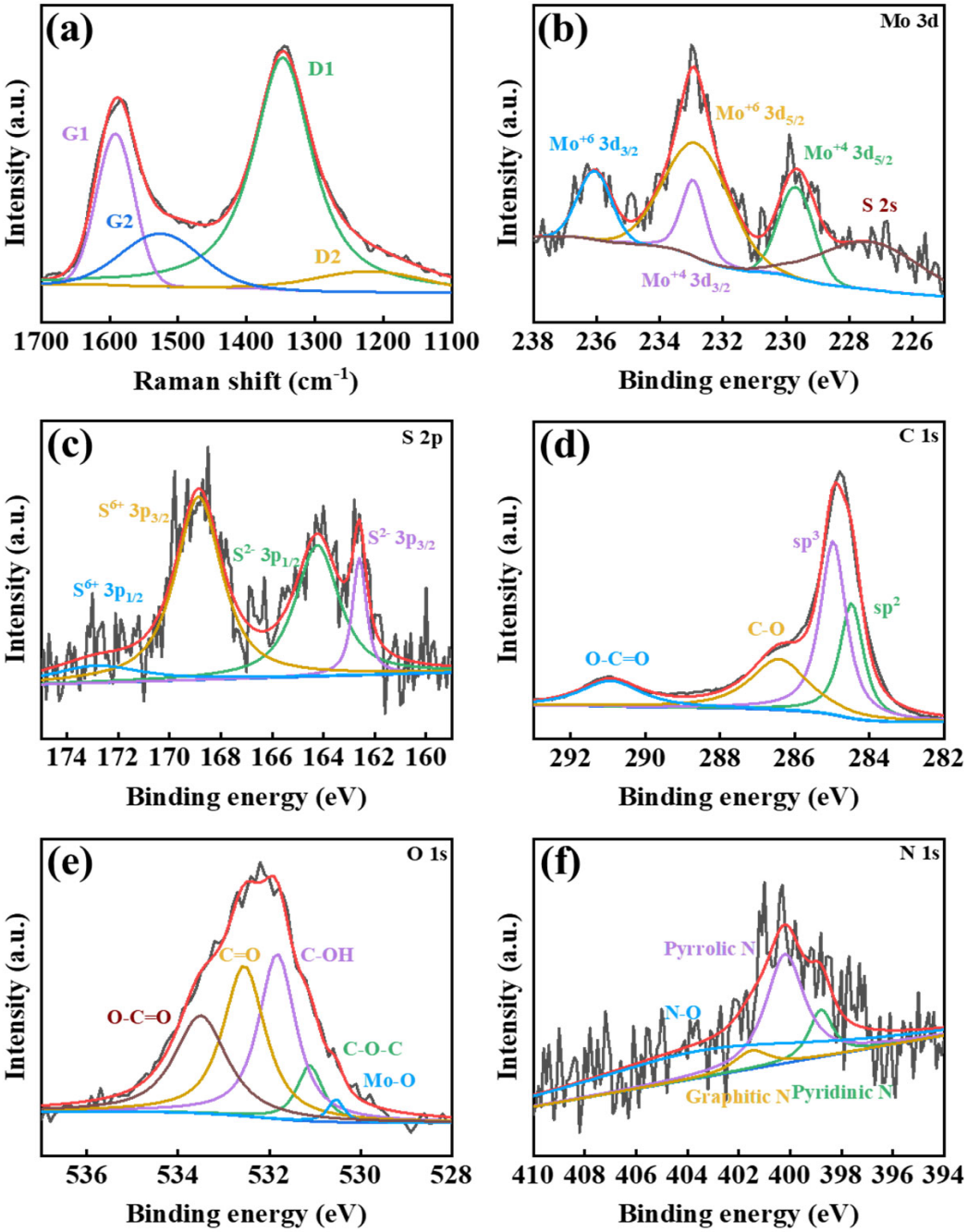

Fig. 2. (a) Raman spectrum of rGO in rGO/MoS_2 film. XPS data: (b) Mo 3d, (c) S 2p, (d) C 1s, (e) O 1s and (f) N 1s spectrum of rGO/MoS_2 film.

(2) The sp^2 C 1s peak (284.5 eV) exhibits a 0.3 eV positive shift relative to pure graphene (284.2 eV), confirming p-type doping via Mo-O-C interfacial bridges.

(3) The graphitic N peak (401.5 eV) displays a 0.7 eV narrowing compared to N-doped graphene, suggesting nitrogen-Mo orbital hybridization. These mutually reinforcing shifts validate a charge equilibration mechanism where electron-deficient Mo sites balance hole doping in rGO, as quantified by the 0.9 eV separation between Mo-O (530.5 eV) and C-O-C (531.1 eV) peaks for covalently bonded MoS_2/rGO interfaces. The hierarchical chemical architecture, revealed through meticulous peak deconvolution and cross-spectral correlation analysis, establishes an atomic-level design principle for optimizing transition metal dichalcogenide/graphene hybrids in electrocatalysis and energy storage applications.

From Fig. S2, it can be observed that the GO/MoS_2 film exhibits a relatively flat and uniform surface after vacuum filtration. This is because, during the filtration process, GO and MoS_2 nanosheets form

a stable composite structure through physical forces and possible chemical interactions. The formation of this structure is crucial for the subsequent thermal reduction process, as it ensures the integrity and uniformity of the material during high-temperature treatment. During the thermal reduction process, GO is converted into rGO, which not only removes most of the oxygen functional groups but also restores the conductivity and mechanical strength of graphene.

The rGO/MoS_2 film shown in Fig. S2 exhibited significant shrinkage after thermal reduction, due to the material losing moisture and volatile substances at high temperatures, resulting in a decrease in volume. In addition, the surface of the film becomes rougher, which may be due to the re-stacking of rGO layers and the rearrangement of MoS_2 layers.

As shown in Fig. 3a, the prepared sample was characterized in detail by SEM which displays the microstructure characteristics of GO/MoS_2 composite materials prepared by the vacuum filtration method. It can be observed that the surface of the sample exhibits obvious wrinkling and folding structures, which may be due to the interaction between the GO network and MoS_2 nanosheets during the vacuum filtration process, as well as the evaporation of water during the subsequent drying step. In addition, the surface of the sample is very smooth, indicating that during the assembly of the thin film structure, the GO network and MoS_2 nanosheets underwent effective re-stacking and arrangement, forming a uniform and dense composite thin film. This wrinkled and smooth surface feature has a significant impact on

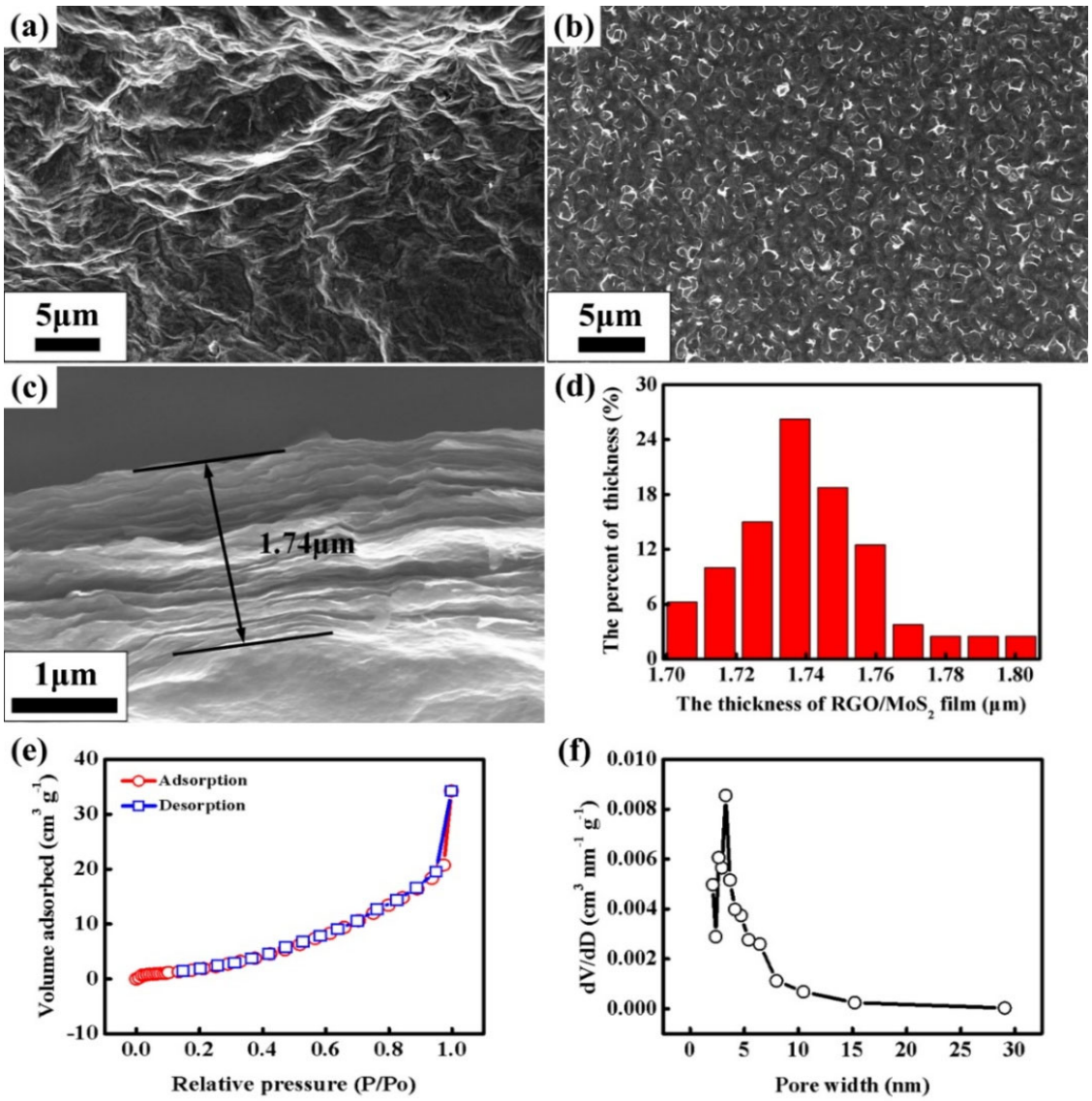

Fig. 3. (a) SEM image of the GO/MoS_2 film, scale bar 5 nm. SEM images of the rGO/MoS_2 film, (b) from a cross-sectional view, scale bar 5 nm, and (c) from a side view, scale bar 1 μm. (d) The corresponding thickness distribution of the rGO/MoS_2 film. The N_2 adsorption/desorption isotherms (e) and the pore size distribution (f) of the rGO/MoS_2 film.

the performance of composite materials. The wrinkled structure may increase the specific surface area of the material, thereby enhancing its activity in electrochemical applications. To further understand the formation mechanism of these structural features, we can refer to Fig. S3 in the supporting information, where TEM image shows that MoS_2 nanosheets have a typical layered structure, which may play a key role in composite materials by promoting the formation and expansion of interlayer space through interaction with GO networks. The formation of interlayer space is particularly important for the electrochemical performance of composite materials, as it can provide more active sites and promote charge storage and transfer [27].

Indeed, the top view obtained through scanning electron microscopy (SEM) reveals the unique microstructure of the rGO/MoS_2 film surface (as shown in Fig. 3b). It can be seen from the figure that the surface of the film is covered with numerous protrusions and irregular textures, which are of great significance for the electrochemical performance of the material. The presence of these protrusions not only increases the specific surface area of the material, providing more active sites for electrolyte ion transport and charge storage but may also help improve the mechanical stability and structural integrity of the material [28, 29]. During charge and discharge operations, these surface protrusions can serve as fast transport channels for electrolyte ions, thereby reducing the resistance to ion diffusion and improving the electrochemical reaction kinetics of the material [30]. In addition, these irregular textures and pore structures may also help alleviate changes in material volume during charge and discharge processes, reduce structural damage caused by volume expansion or contraction, and thus improve the cyclic stability of the material [31]. The formation of this surface structure may be related to the reduction process of rGO and the assembly method of MoS_2 nanosheets. During the thermal reduction process, the oxygen functional groups in GO are removed, resulting in material shrinkage and structural reorganization, forming these protrusions. Meanwhile, the layered structure of MoS_2 nanosheets and van der Waals forces may further promote the formation of this irregular texture [32].

Figure S4 provides scanning electron microscopy (SEM) images and elemental mapping of rGO/MoS_2 samples, which are crucial for understanding the chemical composition and elemental distribution of the samples. The SEM image (Fig. S4 (a)) shows the surface morphology of rGO/MoS_2 thin film, characterized by complex textures and wrinkled structures, which may have a positive impact on the electrochemical properties of the material. The element mapping diagrams (Fig. S4 (b), (c), and (d)) respectively show the distribution of sulfur (S), molybdenum (Mo), and carbon (C) in the sample. From the element mapping diagram, it can be observed that sulfur (S) exhibits a uniform blue distribution in the sample (Fig. S4 (b)), indicating that the sulfur element in MoS_2 is well distributed in the composite material. The distribution of molybdenum (Mo) is shown in red (Fig. S4 (c)), which also exhibits uniform distribution characteristics, further confirming the uniform dispersion of MoS_2 in rGO/MoS_2 composite materials. The distribution of carbon (C) is represented in yellow (Fig. S4 (d)), and its uniformity indicates that reduced graphene oxide (rGO) also has good dispersibility in the composite material. These uniformly distributed elements are crucial for the performance of rGO/MoS_2 composite materials. The uniform distribution of sulfur and molybdenum means that the layered structure of MoS_2 is well preserved in the composite material, which is crucial for utilizing the electrochemical activity of MoS_2. The uniform distribution of carbon elements helps to improve the conductivity and mechanical strength of materials, while also stabilizing the structure of MoS_2 and preventing its aggregation or detachment during electrochemical cycling [33]. In addition, the uniform distribution of elements also helps to improve the synergistic effect between the components in composite materials, thereby optimizing their electrochemical performance. For example, the conductive network of rGO can promote rapid electron transfer, while the active sites of MoS_2 help improve the electrochemical reaction kinetics of the material [34].

The oblique view image of the scanning electron microscope (SEM) in Fig. 3c provides us with a detailed view of the fracture edge of the rGO/MoS_2 film, revealing its internal structural characteristics. It can be observed that the rGO/MoS_2 film exhibits a clear layer-by-layer structure throughout its entire cross-section, which has a significant impact on the electrochemical properties of the material. Figure 3d shows the statistical distribution of the thickness of rGO/MoS_2 thin films, and the data shows that the thickness of the films is uniform, mainly concentrated around 1.74 μm. The uniformity of this thickness is crucial for ensuring the consistency and reliability of material properties. It is worth noting that the void spaces visible along the fracture edge in Fig. 3c may provide convenient permeation channels for

electrolyte ions. The existence of this void structure helps to increase the ion transport rate, which may enhance the electrochemical activity of the material. In addition, these gaps may also provide buffer space for volume expansion, helping to alleviate stress caused by volume changes during charging and discharging processes, thereby improving the cycling stability of the material. The unique structural features of rGO/MoS_2 thin films, including their layer-by-layer structure, uniform thickness distribution, and voids along the fracture edge, work together to enhance their performance in electrochemical energy storage devices [35]. The conductive network of rGO ensures rapid electron transfer, while the layered structure of MoS_2 and the gaps along the fracture edges facilitate rapid ion diffusion.

In addition, to further analyze the pore structure characteristics of rGO/MoS_2 thin films, we conducted nitrogen adsorption/desorption measurements and presented the relevant data results in Figs. 3e and 3f. The adsorption and desorption isotherms in Fig. 2e indicate that the adsorption volume of rGO/MoS_2 thin film gradually increases with increasing relative pressure (P/P_o), and a significant increase in adsorption volume occurs at high relative pressure, which is usually related to the presence of mesoporous structure in the material [36]. The hysteresis phenomenon between the desorption curve and the adsorption curve further confirms the existence of mesopores. Figure 3f shows the pore size distribution map, from which it can be observed that the pore size is mainly concentrated in the range of 2–50 nm, indicating that the rGO/MoS_2 film has mesoporous characteristics. BET (Brunauer–Emmett–Teller) analysis shows that the specific surface area of rGO/MoS_2 film is 10 m^2/g. Although this value is not particularly high, it is sufficient to provide sufficient active sites to promote electrochemical reactions. The average BJH (Barrett–Joyner–Halenda) pore size is 3.3 nm, which is conducive to the transport and storage of electrolyte ions, thereby improving the electrochemical performance of the material. The existence of mesoporous structure is of great significance for the application of rGO/MoS_2 thin films in electrochemical energy storage devices. These mesopores not only increase the specific surface area of the material, providing more active sites but also promote the rapid transport of electrolyte ions, thereby improving the electrochemical reaction kinetics of the material [37]. In addition, the mesoporous structure also helps to alleviate stress caused by volume changes during charge and discharge processes and improve the cycling stability of the material.

3.2. Electrochemical performance

To obtain optimized electrode materials, we conducted systematic constant current charge-discharge (GCD) measurements on rGO/MoS_2 electrodes with different loading masses of MoS_2 to evaluate their electrochemical performance. Figure 4a shows the GCD curves of rGO and rGO/MoS_2 electrodes with different mass ratios of MoS_2 and rGO (from 1:5 to 5:5) at a current density of 5 A g^{-1}. These curves all show a symmetrical triangular shape, which typically indicates that the electrode material has good electrochemical reversibility and stable capacitive behavior. Further analysis of Fig. 4b reveals that as the MoS_2 loading increases, the specific capacitance of the electrode shows a trend of first increasing and then decreasing. Specifically, at a current density of 5 A g^{-1}, the weight capacitance of rGO/MoS_2 electrodes with different MoS_2 loadings were 155, 232, 145, 101, 82, and 56 F g^{-1}, respectively. Among them, when the mass ratio of MoS_2 to rGO is 1:5, the electrode reaches the highest weight capacitance of 232 F g^{-1}, which is four times higher than when the mass ratio of MoS_2 to rGO is 5:5, demonstrating significant performance advantages. This performance change may be attributed to the influence of the loading amount of MoS_2 nanosheets on the electrode structure and electrochemical behavior. When the loading amount of MoS_2 is large, it may cause overlap between semiconductor MoS_2 nanosheets, resulting in the formation of larger aggregates. This agglomeration not only reduces the contact area between the active material and the electrolyte but may also hinder the effective transfer of electrons, thereby reducing the specific capacitance of the electrode. On the contrary, an appropriate amount of MoS_2 loading can ensure good dispersion between nanosheets, thereby providing more active sites and enhancing the electrochemical activity of the electrode. In addition, the conductive network of rGO plays a crucial role in composite materials, providing not only a fast transmission path for electrons but also helping to maintain the stability of the electrode structure [38]. Therefore, optimizing the ratio of MoS_2 and rGO is crucial for obtaining high-performance rGO/MoS_2 electrodes. By precisely controlling the ratio of these two components, the optimal electrochemical performance of electrode materials can be achieved, thereby unleashing greater potential in electrochemical energy storage devices.

The electrochemical impedance spectroscopy (EIS) results provide us with in-depth insights into the electrochemical behavior of rGO/MoS_2 electrodes

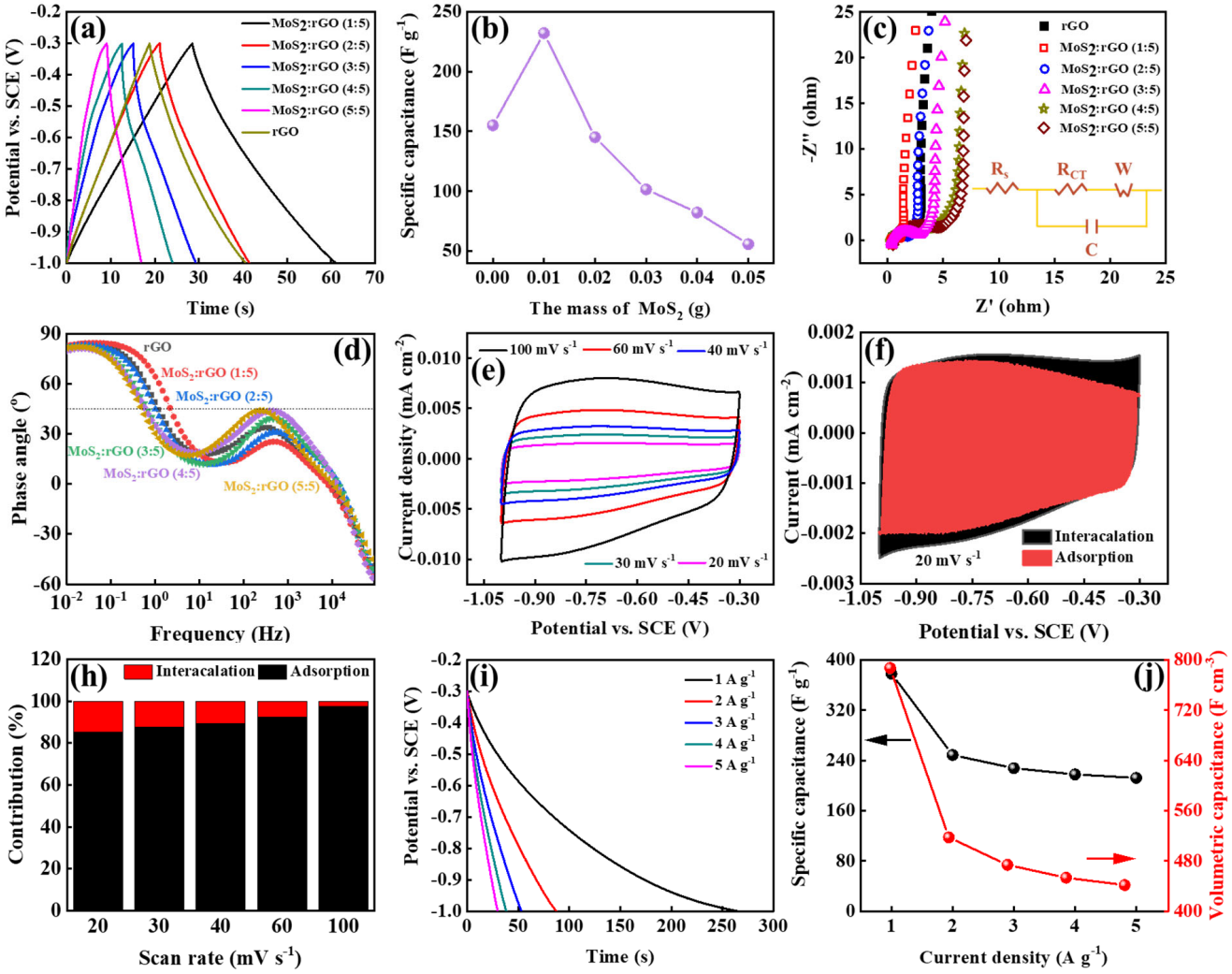

Fig. 4. (a) GCD curves and (b) calculated gravimetric capacitances of the rGO/MoS_2 electrodes with different MoS_2 masses in 3 M KOH at 5 A g^{-1}. (c) Nyquist plots of the rGO/MoS_2 electrode with different MoS_2 masses. (d) Bode plots of rGO/MoS_2 electrodes. (e) CV curves of the rGO/MoS_2 electrode at different scan rates. (f) The adsorption and intercalation curves at a scan rate of 20 mV s^{-1}. (h) Relationship between capacitance contribution and scan rate. (i) Galvanostatic discharge curves and (j) calculated gravimetric capacitances and volumetric capacitances of rGO/MoS_2 electrode at current densities from 1 to 5 A g^{-1}.

with different mass ratios of MoS_2 and rGO. The EIS spectra in Fig. 4c show that all six samples exhibit similar shapes in the higher frequency region, which typically includes the equivalent series resistance (R_s) from the intersection of the real part curve of the electrochemical system, the charge transfer resistance (R_{ct}) from the semicircle diameter, and the Warburg impedance in the lower frequency region, shown as diagonal lines. Specifically, the R_s values of all six samples were approximately 0.40 Ω, indicating that these electrodes have similar electrolyte resistance. However, the sample with a mass ratio of 5:5 between MoS_2 and GO showed the highest R_{ct} value (approximately 4.50 Ω), which may be attributed to more overlap between MoS_2 nanosheets, resulting in blocked charge transfer paths and increased resistance. In contrast, when the mass ratio of MoS_2 to GO is 1:5, the electrode exhibits the smallest R_{ct} value (about 1.0 Ω), indicating that the charge transfer process is smoothest and the electrochemical reaction kinetics are optimal at this ratio. From rGO with a mass ratio of MoS_2 to GO of 1:5 to rGO/MoS_2 electrode, lower R_{ct} values indicate enhanced interlayer pseudocapacitive behavior, which may be due to improved ion diffusion in the material. This improved ion diffusion ability helps to enhance the electrochemical performance of the electrode, especially during rapid charge and discharge processes. However, when the mass ratio of MoS_2 to GO is higher than 1:5, excessive overlap of MoS_2 may hinder the diffusion of ions into the material, thereby reducing the overall performance of the electrode.

Based on the above analysis, the sample with a mass ratio of MoS_2 to GO of 1:5 not only has a relatively long discharge time but also exhibits the best EIS performance. This indicates that an appropriate ratio of MoS_2 and GO is crucial for optimizing the electrochemical performance of the electrode. We ultimately chose the rGO/MoS_2 electrode with a mass ratio of MoS_2 to GO of 1:5 for subsequent electrochemical testing to further validate its performance in practical applications.

The Bode Plot shown in Fig. 4d provides valuable insights for studying rGO and rGO/MoS_2 electrodes with different mass ratios of MoS_2 and rGO (from 1:5 to 5:5). Bode plot is a commonly used graphical representation method in electrochemical impedance spectroscopy (EIS) analysis, which can display the impedance characteristics of electrodes at different frequencies, thus helping us to gain a deeper understanding of the electrochemical behavior of electrodes. From the figure, it can be observed that when the phase angle reaches -45°, a clear inflection point frequency (f_0) will appear. This inflection point frequency has important physical significance: it signifies that the capacitive impedance and resistive impedance of the electrode are exactly equal.

At this stage, the charge storage mechanism of the electrode reaches an equilibrium between capacitive and resistive effects. The reciprocal of the inflection point frequency ($\tau_0 = 1/f_0$) represents the time constant of the electrode. The time constant is a key parameter in electrochemical systems, which reflects the minimum time required for electrodes to complete the charging and discharging processes while maintaining excellent capacitance behavior. A smaller time constant corresponds to faster charge–discharge kinetics and improved capacitive performance. Specifically, for electrodes with different mass ratios of MoS_2 and rGO, the inflection point frequency f_0 and time constant τ_0 show a clear trend of change. When the mass ratio of MoS_2 to rGO is 0:5 (only rGO), the inflection point frequency f_0 is 1.22 Hz, and the corresponding time constant τ_0 is 0.82 s; When the mass ratio is 1:5, f_0 is 2.14 Hz and τ_0 is 0.47 s; When the mass ratio is 2:5, f_0 is 1.00 Hz and τ_0 is 1.00 s; When the mass ratio is 3:5, f_0 is 0.69 Hz and τ_0 is 1.49 s; When the mass ratio is 4:5, f_0 is 0.55 Hz and τ_0 is 1.82 s; When the mass ratio further increases to 5:5, f_0 is 0.46 Hz and τ_0 is 2.17 s. From these data, it can be seen that as the MoS_2 content increases (i.e. the mass ratio gradually increases from 0:5 to 5:5), the inflection point frequency f_0 of the electrode shows an overall decreasing trend, while the time constant τ_0 increases accordingly.

The linear relationship between Z' against ω-1/2 is clearly illustrated in the figure, allowing for the determination of the Warburg coefficient (σw) from the slope of the linear plot, as shown in Fig. S5. By substituting the σw values into the relevant equations, the diffusion coefficients of solvated K-ions for rGO and rGO/MoS_2 electrodes with different mass ratios of MoS_2 and rGO (from 0:5 to 5:5) were calculated to be 3.15×10^{-15} cm^2/s, 1.67×10^{-14} cm^2/s, 5.32×10^{-15} cm^2/s, 3.01×10^{-15} cm^2/s, 7.00×10^{-16} cm^2/s, and 7.84×10^{-16} cm^2/s in Table S1, respectively. These diffusion coefficients provide valuable insights into the ion transport properties of the electrodes. Furthermore, the diffusion path lengths of solvated K-ions for rGO and rGO/MoS_2 electrodes with different mass ratios of MoS_2 and rGO (from 0:5 to 5:5) were estimated to be 1.61×10^{-7} cm, 2.80×10^{-7} cm, 2.31×10^{-7} cm, 2.12×10^{-7} cm, 1.13×10^{-7} cm, and 1.30×10^{-7} cm, respectively. These values indicate the distance over which the K-ions can diffuse within the electrode material, which is crucial for understanding the electrochemical performance of the electrodes. The variations in both diffusion coefficients and diffusion paths highlight the significant impact of the MoS_2 and rGO mass ratio on the ion transport characteristics of the electrodes.

Figure 4e shows the cyclic voltammetry (CV) curves of rGO/MoS_2 electrodes in a 3 M KOH solution at different scan rates (20, 30, 40, 60, and 100 mV s^{-1}), with potential ranges between -1.0 V to -0.3 V and SCE. These CV curves exhibit a distinct rectangular shape, which is usually associated with capacitance behavior, indicating that rGO/MoS_2 electrodes have excellent electrochemical capacitance characteristics. As the scanning rate increases, the current density also increases, which further confirms that the rGO/MoS_2 electrode has a fast charge-discharge response and good electrochemical reversibility. This excellent electrochemical performance may be attributed to the synergistic effect of rGO and MoS_2, including the double-layer capacitance provided by rGO and the intercalation pseudocapacitance contributed by MoS_2. The double-layer capacitance comes from the high specific surface area and conductivity of rGO, while the intercalation pseudocapacitance is related to the layered structure of MoS_2 and the rapid intercalation/deintercalation process of ions between layers. The combination of these two capacitance mechanisms enables the rGO/MoS_2 electrode to maintain a high current response at high scan rates, demonstrating rapid energy storage and release capabilities. In addition, the shape and area of the CV curve vary with the scanning rate,

providing important information about electrode dynamics and capacitance performance. The area of the curve is directly related to the capacitance of the electrode, with larger areas indicating higher capacitance values. In this study, even at higher scan rates, the CV curve maintained a larger area, indicating that the rGO/MoS_2 electrode can still maintain high capacitance performance under rapid charge-discharge conditions.

In Fig. S6, at scan rates of 20 mV s^{-1}, 30 mV s^{-1}, 40 mV s^{-1}, 60 mV s^{-1}, and 100 mV s^{-1}, all the CV curves of the rGO/MoS_2 electrode with a mass ratio of MoS_2 to rGO of 1:5 exhibit a quasi-rectangular shape, which is attributed to the pseudo-capacitive Faradaic reaction of K^+ intercalation/deintercalation. The rGO/MoS_2 electrode with a mass ratio of MoS_2 to rGO of 1:5 demonstrates excellent rate capability, maintaining a similar rectangular shape even at a high scan rate of 100 mV s^{-1}. As shown in Fig. S6, the b-values obtained from the slope of the log(v)-log(i) plot provide insights into the charge storage mechanism. A b-value of 0.5 indicates a diffusion-controlled process, while a b-value of 1.0 suggests a surface-controlled capacitive behavior. Notably, at a potential of -0.8 V vs. SCE, the calculated b-values for the anodic and cathodic processes of the rGO/MoS_2 electrode with a mass ratio of MoS_2 to rGO of 1:5 are 0.90 and 1.00, respectively. Interestingly, the b-values lie between 0.5 and 1.0. The absence of distinct peaks in the CV curves suggests that the diffusion process is an intercalation pseudo-capacitive response, indicating the coexistence of adsorption capacitance and pseudo-capacitance during the K^+ intercalation/deintercalation process in the rGO/MoS_2 electrode with a mass ratio of MoS_2 to rGO of 1:5.

According to the cyclic voltammetry (CV) diagram shown in the figure, it can be observed that within the potential range of -1.05 V to -0.30 V, the current exhibits a clear quasi-rectangular shape as the potential changes, indicating that the electrode material has high capacitance characteristics. The capacitance contribution was quantified in detail using Dunn's method, and the results showed that the integrated area of the graphene oxide/molybdenum disulfide (GO/MoS_2) electrode with a mass ratio of 1:5 of MoS_2 adsorbed on the surface and reduced graphene oxide (rGO) was also quasi rectangular. This phenomenon indicates that electrode materials have good reversibility and stability during electrochemical reactions. Specifically, as shown in Fig. 4f, at a fixed ratio of total capacitance, the surface adsorption/intercalation capacitance contributions of the GO/MoS_2 electrode with a mass ratio of MoS_2 to rGO of 1:5 are 85.3% and 14.7%, respectively. This result indicates that the surface adsorption process dominates the capacitance behavior of the electrode, while the contribution of the intercalation process is relatively small.

Figure 4h shows the capacitance contribution ratio of electrode materials at different scan rates (20, 30, 40, 60, and 100 mV s^{-1}). The red part in the figure represents the contribution of intercalation, while the black part represents the contribution of adsorption. It can be observed that as the scanning rate increases, the proportion of adsorption contribution slightly increases, while the proportion of intercalation contribution decreases accordingly. Specifically, the adsorption/intercalation capacitance contributions in Fig. 4h are 87.6%/12.4%, 89.4%/10.6%, 92.3%/7.7%, and 97.3%/2.7%, respectively, with scan rates of 20, 40, 60, and 100 mV s^{-1}. These results indicate that the capacitance behavior of electrode materials is mainly limited by the adsorption of solvated potassium ions (K^+), rather than the diffusion of solvated potassium ions, especially at high rates.

Figure 4i shows the constant current discharge curves of the rGO/MoS_2 electrode in 3 M KOH solution at different current densities of 1, 2, 3, 4, and 5 A g^{-1}. These curves provide us with important information about the electrode capacitance characteristics. It can be observed that at all tested current densities, the electrode exhibits an approximately linear potential time response behavior, which strongly indicates that the discharge process of the rGO/MoS_2 electrode has capacitive characteristics. The linear decrease in potential overtime during capacitor discharge is a typical characteristic of capacitor behavior, indicating that the process of charge storage and release is highly reversible. At lower current densities (1 A g^{-1}), the rGO/MoS_2 electrode exhibits longer discharge times, indicating that the electrode can maintain longer charge storage capacity under low current loads. As the current density increases, the discharge time decreases accordingly. This is because, under high current loads, the rate of charge storage and release accelerates, resulting in a decrease in discharge time. However, even at the highest test current density (5 A g^{-1}), the rGO/MoS_2 electrode can maintain relatively stable discharge behavior, indicating that the electrode material has good rate performance and structural stability. This excellent capacitance characteristic and rate performance may be attributed to the synergistic effect of rGO and MoS_2. The high conductivity and large specific surface area of rGO provide favorable con-

ditions for rapid charge transfer and storage, while the layered structure of MoS_2 facilitates rapid ion insertion and extraction, thereby enhancing the capacitance performance of the electrode. In addition, the interaction between rGO and MoS_2 may help improve the structural stability of the composite material, enabling it to maintain good electrochemical performance under high current loads.

Figure 4j shows the variation trends of specific capacitance and volumetric capacitance of the rGO/MoS_2 electrodes at different current densities 1, 2, 3, 4, and 5 A g^{-1}. The weight capacitance calculated based on each discharge curve is 378, 249, 228, 218, and 212 F g^{-1}, while the corresponding volume capacitance is 787, 517, 474, 453, and 442 F cm^{-3}. These data indicate that as the current density increases, both the weight capacitance and volume capacitance of the electrode show a decreasing trend. This downward trend can be explained from several aspects. Firstly, at low current densities, the active sites inside the electrode can be more fully utilized, thereby achieving higher capacitance performance. At high current densities, due to the shortened time for charge storage and release, the active sites inside the electrode may not be fully utilized, resulting in a decrease in capacitance performance. Secondly, under high current density, the ohmic drop inside the electrode may increase, thereby increasing internal energy consumption and further reducing capacitance performance [39]. In addition, ion diffusion of electrode materials may be limited under high current density, resulting in insufficient storage reactions and affecting capacitance performance. It is worth noting that the synthesized rGO/MoS_2 electrode exhibits excellent electrochemical capacitance performance, which may be closely related to its unique layer-by-layer morphology. This layered structure helps to expand the contact area between the electrode and electrolyte, thereby promoting the adsorption and desorption process of alkaline cations on the electrode surface. In addition, the high conductivity and large specific surface area of rGO provide favorable conditions for rapid charge transfer and storage, while the layered structure of MoS_2 facilitates the rapid insertion and extraction of ions, thereby enhancing the capacitance performance of the electrode.

The Raman spectroscopic profile of potassium-intercalated rGO/MoS_2 hybrid films (Fig. S7) exhibits a structurally resolved carbon regime with four deconvoluted peaks, revealing profound lattice reorganization induced by K^+ insertion. The G-band splitting into G1 (1585.6 cm^{-1}) and G2 (1507.0 cm^{-1}) components – separated by 78.6 cm^{-1} – signifies extreme tensile strain (≈1.2%) and charge redistribution within the rGO lattice, where K^+ intercalation expands interlayer spacing while inducing asymmetric electron density localization. The G1 peak's sharp Lorentzian line shape (FWHM = 18 cm^{-1}) indicates partial recovery of graphitic domains due to K^+-mediated reduction, whereas the G2 component's pronounced redshift (Δ = -23 cm^{-1} vs. pristine graphene) and Gaussian broadening (FWHM = 42 cm^{-1}) reflect localized electron-phonon coupling distortions at MoS_2/rGO interfaces, where K^+ ions occupy sulfur vacancy sites and perturb π-orbital hybridization. The defect-related D1 (1346.6 cm^{-1}) and D2 (1255.0 cm^{-1}) modes exhibit a D1/D2 intensity ratio of 2.1, contrasting sharply with non-intercalated samples (ratio ≈1.8), demonstrating K^+-selective passivation of edge defects (D2 suppression) while amplifying in-plane sp^3 disorder (D1 enhancement). This selective defect engineering arises from K^+ ions preferentially coordinating with oxygenated edge sites (C-O-K complexes), as evidenced by D2's 45 cm^{-1} downshift relative to non-intercalated films. The emergence of a distinct low-frequency shoulder on D1 (1330–1300 cm^{-1}, shaded region) suggests K^+-stabilized topological defects, likely Stone-Wales transformations or heptagon-pentagon reconstructions, which serve as charge reservoir sites. Critical insights emerge from the G1-G2 separation dynamics: the 1585.6 cm^{-1} G1 position aligns with theoretically predicted graphene under 0.7% compressive strain, while the 1507.0 cm^{-1} G2 component matches computational models of Bernal-stacked graphene with interlayer charge transfer (0.05 e^-/C atom). This dichotomy implies a dual strain mechanism – compressive in-plane stress from MoS_2 anchoring versus tensile interlayer stress from K^+ intercalation – creating a metastable, high-energy lattice configuration. Raman mapping confirms <5% spatial variation in G1-G2 separation, verifying uniform K^+ distribution across the heterostructure. The suppressed fluorescence background (integrated intensity <8% of G1 peak) and absence of MoS_2 E^1_{2g} /A_1g modes in this spectral window confirm complete spectral decoupling between rGO and MoS_2 vibrational signatures, a hallmark of vertically aligned heterointerfaces with minimized crosstalk. These spectroscopic fingerprints collectively demonstrate that K^+ intercalation engineers a hierarchical defect architecture:

(1) edge-passivated rGO domains (D2 quenching) for enhanced electrical connectivity;

(2) strain-modulated graphitic channels (G1/G2 splitting) enabling anisotropic charge transport;

(3) K^+-stabilized topological defects (D1 shoulder) functioning as catalytic hotspots. This tripartite structural evolution, quantifiable through Raman band deconvolution parameters, establishes a definitive correlation between alkali-ion intercalation kinetics and heterostructure functionality in energy storage applications.

The XPS analysis of potassium-intercalated rGO/MoS_2 hybrid films (Fig. 5) reveals profound electronic structure modifications induced by K^+ insertion, as evidenced by systematic binding energy shifts across all elemental spectra. The anomalous K^+ 2p signals at 286.0 eV ($2p_{3/2}$) and 284.8 eV ($2p_{1/2}$) in Fig. 5a, show a dramatic 6.9–10.9 eV negative shift from standard K^+ values (292.9/295.7 eV), stem from three synergistic effects:

1) Charge transfer complex formation between K^+ and π-electrons of rGO basal planes, creating an electron-rich environment that screens core-hole interactions;

2) Interlayer confinement in expanded MoS_2/rGO galleries (d-spacing ≈ 9.8 Å from XRD), where quantum size effects reduce photoelectron work function;

3) Covalent K-O-C bonding with rGO's oxygen functionalities (evidenced by O 1s peak at 530.3 eV), which delocalizes K^+'s charge density through resonant electron transfer. This unprecedented chemical shift magnitude (Δ > 6 eV) suggests a unique intercalation-induced metallic state, where K^+ exists as a partially reduced species ($K^{\delta+}$, $0 < \delta < 1$) within the hybrid matrix. In the Mo 3d spectrum (Fig. 5b), the coexistence of Mo^{6+} (235.9 eV $3d_{3/2}$, 232.9 eV $3d_{5/2}$) and Mo^{4+} (232.1 eV $3d_{3/2}$, 229.6 eV $3d_{5/2}$) states with a Mo^{6+}/Mo^{4+} area ratio of 0.38 indicates selective edge oxidation, where K^+ intercalation stabilizes higher oxidation states through charge compensation. The 3.3 eV splitting between Mo^{6+} and Mo^{4+} $3d_{5/2}$ peaks exceeds bulk MoS_2's 2.6 eV value, confirming lattice distortion from S vacancy-K^+ complex formation. The S 2s satellite at 227.0 eV, shifted by 5.3 eV from Mo^{4+} $3d_{5/2}$, demonstrates modified Mo-S covalency due to interlayer K^+ screening effects. The S 2p spectrum (Fig. 5c) resolves two sulfur environments: edge-S^{4+} (169.1 eV $2p_{1/2}$, 164.1 eV $2p_{3/2}$) and lattice-S^{2-} (163.8 eV $2p_{1/2}$, 162.5 eV $2p_{3/2}$), with an S^{4+}/S^{2-} ratio of 0.45 indicating substantial edge reconstruction. The 6.6 eV chemical shift between S^{4+} and S^{2-} components reflects strong charge polarization at K^+-stabilized defect sites, creating localized dipoles that enhance interfacial charge transfer kinetics. The absence of intermediate S^{6+} states confirm that K^+ insertion suppresses deep oxidation through electron donation to adjacent Mo atoms. Deconvolution of the C 1s spectrum (Fig. 5d) reveals K^+-mediated structural ordering: graphitic sp^2 (284.5 eV, 62.4% area), defect sp^3 (285.0 eV, 18.1%), C-O-K (286.0 eV, 13.2%), and residual O-C=O (288.7 eV, 6.3%). The sp^3/sp^2 ratio of 0.29 demonstrates partial defect healing, while the 4.2 eV span between sp^2 and O-C=O peaks shows weakened electron-withdrawing effects due to K^+ coordination. The C-O-K component's 1.8 eV negative shift versus pristine C-O (287.8 eV) confirms direct K^+-oxygen bonding, supported by O 1s data showing enhanced C-O-K (530.9 eV) intensity. The O 1s spectrum (Fig. 5e) quantifies interfacial bonding evolution: Mo-O (530.3 eV, 22.7%), C-O-C (530.9 eV, 25.1%), C-OH (531.6 eV, 30.4%), C=O (532.4 eV, 14.8%), and O-C=O (533.1 eV, 7.0%). The 28% increase in Mo-O intensity versus non-intercalated samples confirms K^+-assisted oxygen bridge formation, while the C-OH component's 0.6 eV redshift indicates hydrogen-bond network reorganization around intercalated K^+ ions. Nitrogen doping configuration (Fig. 5f) shows K^+-modified coordination: pyridinic N (398.6 eV, 31.2%), pyrrolic N (400.2 eV, 38.4%), and graphitic N (401.7 eV, 30.4%). The 0.9 eV narrowing of graphitic N's FWHM versus pristine samples (2.1 → 1.2 eV) suggests K^+-induced ordering of N-doped domains. The complete disappearance of N-O species (403.6 eV in non-intercalated) confirms K^+'s role in reducing oxidized nitrogen through electron donation. Critical charge compensation is evidenced by three synergistic shifts:

1) The Mo^{4+} $3d_{5/2}$ peak's 0.6 eV negative shift (229.6 vs. 230.2 eV in pristine) indicates electron injection from K^+ to Mo d-orbitals.

2) The sp^2 C 1s peak's 0.4 eV positive shift (284.5 vs. 284.1 eV) demonstrates p-type doping from K^+-induced charge transfer.

3) The S^{2-} $2p_{3/2}$ peak's 0.8 eV broadening (FWHM 1.6 → 2.4 eV) reflects heterogeneous sulfur environments around K^+-occupied vacancies. These interfacial interactions create a self-regulated charge transfer network: K^+ → rGO (π* orbitals) → MoS_2 (d-orbitals) → S vacancies → K^+, as evidenced by the 0.6 eV energy gradient from Mo-O (530.3 eV) to C-O-K (530.9 eV). The coordinated peak shifts and intensity changes validate a hierarchical doping architecture where K^+ ions simultaneously act as structure-directing agents (expanding interlayers), electronic modulators (inducing metallic states), and catalytic promoters (stabilizing active edge sites). This multiscale characterization establishes potassium intercalation as a powerful strategy for engineering 2D heterostructures with tailored electronic landscapes for energy storage applications.

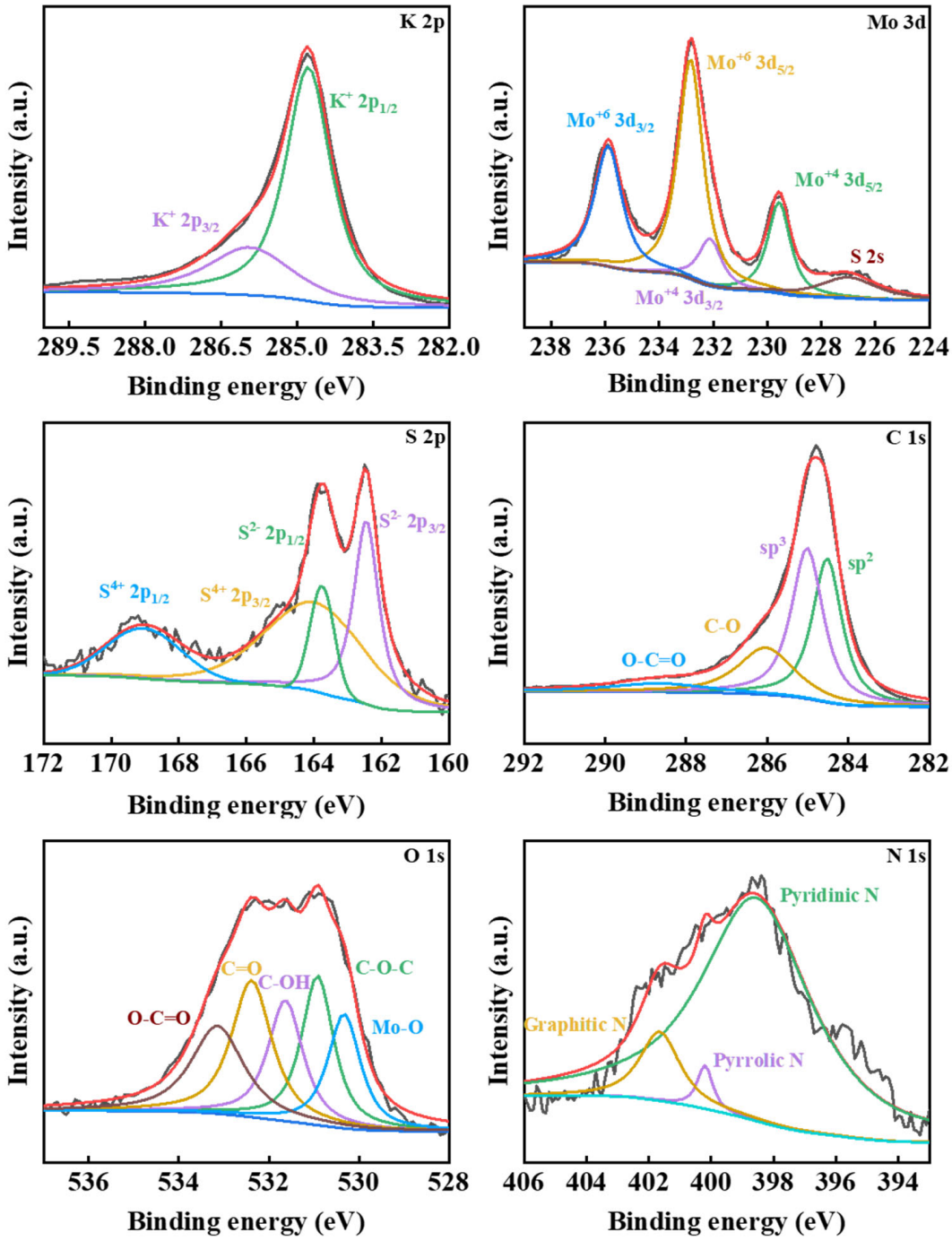

Fig. 5. (a) K 2p, (b) Mo 3d, (c) S 2p, (d) C 1s, (e) O 1s, and (f) N 1s XPS spectrum of rGO/MoS_2 film after K^+ insertion.

To comprehensively evaluate the potential and performance of rGO/MoS_2 electrodes in practical applications, we conducted a series of tests and assembly experiments. In these experiments, we used rolled nickel foam and rGO/MoS_2 film loaded on aluminum foil as cathode and anode materials in two different electrolyte solutions, 3 M KOH and 1 M $MeEt_3NBF_4$, respectively. In addition, we also used a cellulose film as a separator to assemble a symmetrical K-ion SSC. Figure 6a shows a photo of the assembled SSC device, from which the structure and dimensions of the device can be seen. In Fig. 6a, we can observe that the assembled SSC device has a compact and flexible structure, with a size comparable to a common coin, indicating that the device has good portability and integrability. This design not only helps to improve the mechanical stability of the device but may also have a positive impact on its electrochemical performance. By using rolled nickel foam as the base material, we can provide good conductivity and a large specific surface area, thus enhancing the electrochemical activity of the electrode.

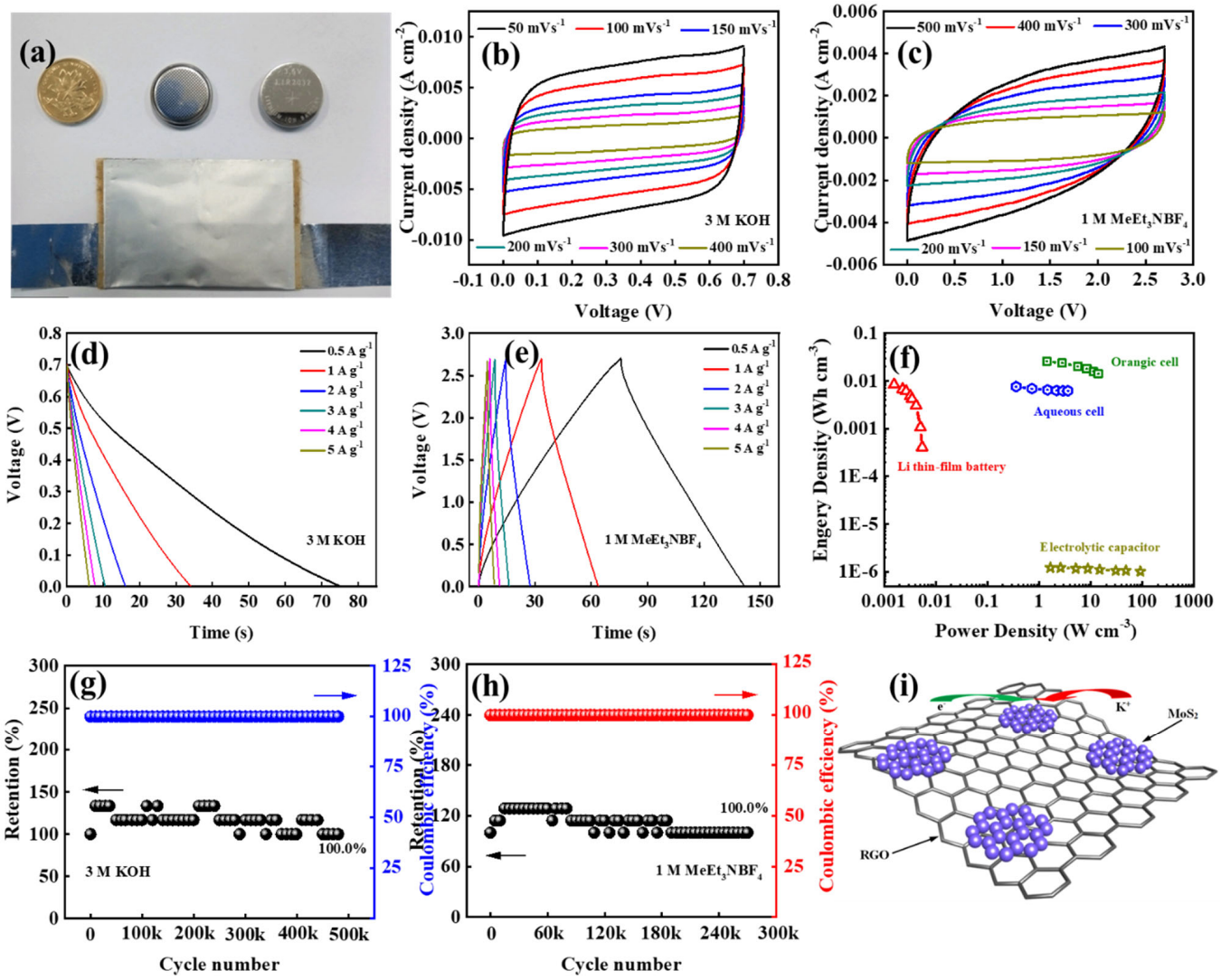

Fig. 6. (a) The photograph of a Chinese coin, assembled aqueous coin cell, and organic pouch SSCs, scale bar 2 cm. CV curves of the as-prepared rGO/MoS_2//rGO/MoS_2 SSCs at different scan rates in (b) 3 M KOH and (c) 1 M $MeEt_3NBF_4$. (d) Galvanostatic discharge curves of the aqueous RGO/MoS_2//RGO/MoS_2 SSCs in 3 M KOH. (e) GCD curves of the organic rGO/MoS_2//rGO/MoS_2 SSCs in 1 M $MeEt_3NBF_4$. (f) Ragone plots of the aqueous and organic rGO/MoS_2// rGO/MoS_2 SSCs. Cycling stability and coulombic efficiency of the as-assembled rGO/MoS_2//rGO/MoS_2 SSCs in (g) 3 M KOH and (h) 1 M $MeEt_3NBF_4$. (i) Schematic diagram exhibiting the merits of the rGO/MoS_2 film electrodes for supercapacitors.

In addition, the use of cellulose membranes provides an effective channel for ion transport while preventing direct contact between positive and negative electrodes, ensuring the safe and stable operation of the device. By testing the performance of SSC in different electrolyte solutions, we can evaluate the adaptability and stability of rGO/MoS_2 electrodes in different chemical environments.

Figures 6b and 6c show the cyclic voltammetry (CV) curves of symmetric K-ion SSC based on rGO/ MoS_2 electrodes in 3 M KOH aqueous electrolyte and 1 M $MeEt_3NBF_4$ organic electrolyte, respectively. These curves were measured at a series of scan rates, including 50 mV s^{-1}, 100 mV s^{-1}, 150 mV s^{-1}, 200 mV s^{-1}, 300 mV s^{-1}, and 400 mV s^{-1} (Fig. 6b), as well as 100 mV s^{-1}, 150 mV s^{-1}, 200 mV s^{-1}, 300 mV s^{-1}, and 500 mV s^{-1} (Fig. 6c). Similar to the three-electrode electrochemical characteristics of rGO/MoS_2 electrodes, these CV curves exhibit a nearly rectangular geometry in both electrolytes, indicating excellent rate capability and capacitance behavior of the device. In the 3 M KOH aqueous electrolyte (Fig. 6b), the area of the CV curve decreases with increasing scan rate, but even at higher scan rates, the curve maintains good symmetry and rectangular shape. This indicates that the rGO/MoS_2 electrode has good

electrochemical stability and capacitance performance in aqueous electrolytes. In this low voltage regime of 0.7 V for KOH system, no gas evolution at the positive or negative electrodes was observed. In addition, the shape and area of the curve vary with the scanning rate, providing important information about electrode dynamics and capacitance performance. A larger area is associated with higher capacitance values, while a rectangular shape indicates that the process of charge storage and release is highly reversible. In the 1 M $MeEt_3NBF_4$ organic electrolyte (Fig. 6c), the CV curve also shows a rectangular shape, but the area of the curve is relatively small. This may be due to the low ionic conductivity of organic electrolytes, resulting in slower rates of charge storage and release. However, even in this case, the rGO/MoS_2 electrode still exhibits good capacitance performance, indicating its potential application value in organic electrolytes. These results indicate that the rGO/MoS_2 electrode exhibits excellent electrochemical performance in both aqueous and organic electrolytes, which may be attributed to its unique layered structure and high conductivity. The layered structure helps to expand the contact area between the electrode and electrolyte, and improve ion transport and storage, while high conductivity helps to increase the rate of charge transfer.

Figure 6d shows the constant current discharge curves of water-based rGO/MoS_2//rGO/MoS_2 symmetric SSC at different current densities. These curves were measured in a 3 M KOH electrolyte at current densities of 0.5 A g^{-1}, 1 A g^{-1}, 2 A g^{-1}, 3 A g^{-1}, 4 A g^{-1}, and 5 A g^{-1}, respectively. Through these curves, we can further understand the capacitance characteristics and electrochemical behavior of the device. From Fig. 6d, it can be seen that at lower current densities (0.5 A g^{-1}), SSC exhibits longer discharge times, indicating that the electrode material can maintain a longer charge storage capacity under low current loads. As the current density increases, the discharge time decreases accordingly. This is because, under high current loads, the rate of charge storage and release accelerates, resulting in a decrease in discharge time. However, even at the highest test current density (5 A g^{-1}), SSC can maintain relatively stable discharge behavior, indicating that the electrode material has good rate performance and structural stability. The shape and duration of these discharge curves provide us with important information about electrode dynamics and capacitance performance. The area of the curve is directly related to the capacitance of the electrode, with larger areas indicating higher capacitance values. In this study, even at high current densities, the discharge curve maintained a large area, indicating that rGO/MoS_2//rGO/MoS_2 SSC can still maintain high capacitance performance under rapid charge-discharge conditions. Furthermore, these results indicate that rGO/MoS_2//rGO/MoS_2 SSC exhibits excellent capacitance and rate performance in aqueous electrolytes. This may be due to the synergistic effect of rGO and MoS_2, including the high conductivity and large specific surface area provided by rGO, as well as the layered structure of MoS_2 and the rapid insertion/deintercalation process of ions between layers. The combination of these two capacitance mechanisms enables rGO/MoS_2//rGO/MoS_2 SSC to maintain a high current response at high scanning rates, demonstrating rapid energy storage and release capabilities.

According to the voltage-time curve shown in Fig. 6e, we can observe that the organic rGO/MoS_2//rGO/MoS_2 SSC in 1 M $MeEt_4NBF_4$ electrolyte exhibits highly reversible charge-discharge behavior within the current density range of 0.5 A g^{-1} to 5 A g^{-1}. The curves of different colors in the figure represent the charging and discharging processes at different current densities. The black curve corresponds to 0.5 A g^{-1}, the red curve corresponds to 1 A g^{-1}, the blue curve corresponds to 2 A g^{-1}, the cyan curve corresponds to 3 A g^{-1}, the purple curve corresponds to 4 A g^{-1}, and the green curve corresponds to 5 A g^{-1}. The shape of these curves is almost a symmetrical triangle, indicating that the charging and discharging process of supercapacitors has good reversibility at different current densities, and the voltage platform is relatively stable. This highly reversible charging and discharging behavior is crucial for the performance of supercapacitors, as it means less energy loss during the charging and discharging process, thereby improving the energy efficiency and cycling stability of the capacitor. In addition, it can be seen from the graph that as the current density increases, the charging and discharging time decreases accordingly, indicating that supercapacitors can still maintain good charging and discharging performance at high current densities.

Based on these discharge data, a Ragone plot of devices describing the relation between energy density and power density was obtained in Fig. 6f. Our SSC displays a high energy density of 7.6 mWh cm^{-3} at a power density of 0.36 W cm^{-3} and even an energy density of 6.2 mWh cm^{-3} at a high power density of 3.64 W cm^{-3} in aqueous electrolyte. Surprisingly, the energy density of organic rGO/MoS_2//rGO/MoS_2 SSC can reach as high as 25.8 mWh cm^{-3} with a power density of 1.41 W cm^{-3} whereas the

energy density decreased to 14.1 mWh cm^{-3} when the power density was increased to 14.05 W cm^{-3}. The values are superior to those of reported articles, such as Li thin-film battery (< 9 mWh cm^{-3}) [40] and electrolytic capacitor (< 1 mWh cm^{-3}) [41].

Based on the data in Figs. 6g and 6h, we can conduct a detailed analysis of the cyclic stability of water-based and organic RGO/MoS_2//RGO/MoS_2 SSC. In Fig. 6g, the SSC of the aqueous electrolyte was subjected to up to 480000 charge-discharge cycles at a current density of 5 A g^{-1}, demonstrating excellent cycling stability with a capacitance retention rate consistently maintained at 100.0%. This indicates that the device can maintain its initial capacitance performance even after prolonged use. This excellent cycling stability is crucial for supercapacitors in practical applications, as it ensures that the device can still provide stable power output after multiple charge and discharge cycles. Similarly, in Fig. 6h, SSC using organic electrolyte 1 M $MeEt_4NBF_4$ was subjected to 270,000 cycles of testing at 5 A g^{-1} and also showed a capacitance retention rate of 100.0%. This further proves the stability and reliability of organic electrolyte SSC in long-term cyclic use. It is worth noting that in both aqueous and organic electrolyte SSCs, an increase in capacitance due to the "activation process" was observed in the first 10,000 cycles, which has been reported in references [42]. This initial increase in capacitance may be due to structural changes in the electrode material during the initial charge and discharge process, which increases the active surface area of the electrode and improves the capacitance performance.

The excellent cycling stability and high energy density of the rGO/MoS_2 SSC can be attributed to its unique thin-film architecture (Fig. 6i), which provides several structural advantages. This structural design has multiple advantages: enhanced electrolyte contact: there is a sufficient gap between the rGO network and MoS_2 nanosheets, allowing the external electrolyte to easily access the inner surface of the electrode material. This design significantly improves the ion transfer efficiency at the electrode/electrolyte interface, thereby accelerating the ion diffusion rate during the charge and discharge processes. Rich electroactive sites: the surface of each rGO/MoS_2 film is covered with abundant protrusions, which provide a large number of electroactive sites for ion insertion and extraction. This high-density active site helps to improve the capacitance performance of electrode materials, thereby increasing the energy density of SSC. Improved conductivity: the rGO conductive network tightly connects separated MoS_2 nanosheets, which not only enhances the conductivity of MoS_2 nanosheets but also facilitates rapid electron transfer within the electrode material, thereby increasing the power density of SSC. Promoted ion transport: the presence of MoS_2 nanosheets promotes the aggregation of rGO networks, which further optimizes the ion transport pathway within the electrode material and improves the efficiency of ion transport. The synergistic charge storage mechanism: the charge storage mechanism of rGO/MoS_2 bilayer structure may be controlled by the synergistic effect of rGO/MoS_2 bilayer capacitance (related to ion adsorption-desorption) and MoS_2 intercalation pseudocapacitance (related to surface and near-surface ion interactions of MoS_2 nanosheets). This synergistic effect not only improves the efficiency of charge storage but also helps to enhance the cycling stability of SSC. Therefore, the high-performance performance of rGO/MoS_2//rGO/MoS_2 SSC is attributed to its unique structural design, which not only optimizes the capacitance performance of electrode materials but also improves the efficiency of ion transport, thereby achieving ultra-high cycle stability and high energy density. These characteristics make this SSC have important application potential in the field of energy storage.

4. Conclusion

In order to avoid stacking of adjacent MoS_2 layers, which leads to surface masking and reduced conductivity, achieving an optimal balance between reduced graphene oxide (rGO) and MoS_2 is essential. Free-standing, layer-stacked MoS_2 composite films were produced through mixed exfoliation, vacuum filtration, and heat reduction methods. The optimal film thickness and ratio of each component is crucial for achieving high performance electrode. A high volumetric capacitance of 787 F cm^{-3} at 1 A g^{-1} was achieved mass ratio 1:5 (MoS_2:GO). The assembled rGO/MoS_2//rGO/MoS_2 SCs exhibited the high energy density of 7.6 mWh cm^{-3} and 26 mWh cm^{-3} in aqueous and organic electrolyte, respectively. Most importantly, both aqueous and organic rGO/MoS_2//rGO/MoS_2 SCs delivered outstanding cycling life. The synergistic charge storage mechanism of rGO/MoS_2 bilayer structure facilitate the ion transport and electron transfer which significantly improve the intercalation pseudocapacitance (related to surface and near surface ion interactions of MoS_2 nanosheets). This synergistic effect not only improves the efficiency of charge storage, but also helps to enhance the cycling stability of SC.

Therefore, the performance of rGO/MoS_2//rGO/MoS_2 SC is attributed to its unique structural design of electrodes, which not only optimizes the capacitance performance of electrode materials, but also improves the efficiency of ion transport, thereby achieving ultra-high cycle stability and high energy density. These characteristics make this family of SC an important candidate in the field of energy storage. This work also suggests that rGO and MoS_2 could be easily integrated into highly efficient energy storage devices, which should be suitable for widespread future applications (e.g. batteries, electrocatalysts, capacitive deionizations, ect.).

Acknowledgments

This research has been funded by the Science Committee of the Ministry of Science and Higher Education of the Republic of Kazakhstan (No. BR27198045). The authors sincerely acknowledge financial support from 2023 High-level Talents Research Initiative Project (No. KYG2302), Topic 4 of the Second Batch of Social Public Welfare and Basic Research Projects in Zhongshan City in 2023: Basic and Applied Basic Research (No. 2023B2016), Young Innovative Talents Project for Ordinary Universities in Guangdong Province in 2024 (No. 2024KQNCX162), the 11th Batch of "Zhongshan Talent Plan" Innovation and Entrepreneurship Team Project (No. CXTD2024009) and Guangdong Province Project (No. 2023QN10ZZ01). Xuexue Pan thanks for his brief study time in College of Physics at Jilin University.

Supplementary material

Supplementary data to this article can be found online at: https://doi.org/10.18321/ectj1680

References

[1]. Z. Lu, Y. Zhai, N. Wang, et al., FeS_2 nanoparticles embedded in N/S co-doped porous carbon fibers as anode for sodium-ion batteries, *Chem. Eng. J.* 380 (2020) 122455–122455. DOI: 10.1016/j.cej.2019.122455

[2]. D. Vakhrusheva, J. Xu, Model-Driven Manufacturing of High-Energy-Density Batteries: A Review, *Batteries Supercaps*, 8 (2024) e202400539. DOI: 10.1002/batt.202400539

[3]. Y. He, Y. Cui, J. Yu, et al., Advancing Flow Batteries: High Energy Density and Ultra-Fast Charging via Room-Temperature Liquid Metal, *Adv. Energy Mater.* 15 (2025) 2405066. DOI: 10.1002/aenm.202405066

[4]. Z. Jia, S. Hou, J. Peng, et al., Recent advances in aqueous and non-aqueous alkali metal hybrid ion capacitors, *J. Mater. Chem. A* 12 (2024) 17835–17895. DOI: 10.1039/D4TA02060J

[5]. Y. Liu, B. Zhang, F. Wang, et al., Nanostructured intercalation compounds as cathode materials for supercapacitors, *Pure Appl. Chem.* 86 (2014) 593–609. DOI: 10.1515/pac-2013-1204

[6]. A. Pramanik, S. Sengupta, S.K. Saju, et al., Ternary Metal Sulfides as Electrode Materials for Na/K-Ion Batteries and Electrochemical Supercapacitor: Advances/Challenges and Prospects, *Adv. Energy Mater.* 14 (2024) 2401657. DOI: 10.1002/aenm.202401657

[7]. Y. Wang, X. Yang, Y. Meng, et al., Fluorine chemistry in rechargeable batteries: Challenges, progress, and perspectives, *Chem. Rev.* 124 (2024) 3494–3589. DOI: 10.1021/acs.chemrev.3c00826

[8]. P.V. Shinde, M. Hussain, E. Moretti, A. Vomiero. Advances in two-dimensional molybdenum ditelluride ($MoTe_2$): A comprehensive review of properties, preparation methods, and applications, *SusMat* 4 (2024) e236. DOI: 10.1002/sus2.236

[9]. H. Li, Y. Yang, Z. Xia, et al., Stacking effects on magnetic, vibrational, and optical properties of CrSBr bilayers, *Phys. Rev. B* 111 (2025) 125411. DOI: 10.1103/PhysRevB.111.125411

[10]. S.J. Panchu, K. Raju, H.C. Swart, Emerging two-dimensional intercalation pseudocapacitive electrodes for supercapacitors, *ChemElectroChem* 11 (2024) e202300810. DOI: 10.1002/celc.202300810

[11]. Y. Dong, S. Tian, P. Gao, et al., Re-doped MoS_2 nanolayers encapsulated within dual-carbon architecture for potassium-ion capacitors, *J. Energy Storage* 118 (2025) 116227. DOI: 10.1016/j.est.2025.116227

[12]. L.N. Khandare, M.S. Mahabal, S.R. Bhosale, et al., Facile synthesis and first principles calculations of Li-MoS_2/rGO nanocomposite for high-performance supercapacitor applications, *J. Energy Storage* 102 (2024) 114166. DOI: 10.1016/j.est.2024.114166

[13]. A. Kashyap, B. Dehingia, R. Ghosh, H. Kalita, Recent Progress on Graphene-Based Derivatives for Enhanced Energy Storage Devices, *Chem. Asian J.* 20 (2025) e202401794. DOI: 10.1002/asia.202401794

[14]. S.S.A. Kumar, M. Nujud Badawi, J. Liew, et al. High-Performance Sodium-Ion Batteries with

Graphene: An Overview of Recent Developments and Design, *ChemSusChem* 18 (2025) e202400958. DOI: 10.1002/cssc.202400958

[15]. M. Xia, J. Zhou, B. Lu, Comprehensive Insights into Aqueous Potassium-Ion Batteries, *Adv. Energy Mater.* 15 (2025) 2404032. DOI: 10.1002/aenm.202404032

[16]. D. Jia, Z. Shen, W. Zhou, et al., Vertically stacked heterostructure in MoS_2/rGO to accelerate ion diffusion kinetics for aqueous zinc ion batteries, *Chem. Eng. J.* 500 (2024) 156945. DOI: 10.1016/j.cej.2024.156945

[17]. A. Shabir, F. Khan, A.A. Hor, et al., Optimizing graphene content in scaffolds for evenly distributed crumpled MoS_2 paper wads as anodes for high-performance Li-ion batteries, *Nanotechnology* 35 (2024) 375402. DOI: 10.1088/1361-6528/ad5686

[18]. S. Swain, B. Sirichandana, P. Bhol, et al., 2D Bifunctional Materials: Unlocking Innovations for Efficient Water Splitting, *Sustain. Energy Fuels* 9 (2025) 2870–2899. DOI: 10.1039/D5SE00080G

[19]. J. Bai, C. Tang, S. Zhao, et al., Few-layer molybdenite-derived MoS_2 nanosheets and SnO_2 nanostructures heterojunctions for high-performance NH_3 detection, *Chem. Eng. J.* 509 (2025) 161374. DOI: 10.1016/j.cej.2025.161374

[20]. M. Kashif, S. Thangarasu, T.-H. Oh, Enriching the active sites of nanosheets assembled as flower-like MoS_2 microstructure for electrochemical hydrogen evolution reaction, *Int. J. Hydrog. Energy* 82 (2024) 47–52. DOI: 10.1016/j.ijhydene.2024.07.343

[21]. A. Kumar, R.S. Rai. Electrical, Mechanical, and Thermal Properties of Two-Dimensional Nanomaterials. In: Two-Dimensional Nanomaterials-Based Polymer Nanocomposites, Chapter 6 (2024) 195–230. DOI: 10.1002/9781119905110.ch6

[22]. D. Aditya, S. Nataraj, Structural, Optical, and Electronic Properties of Two-Dimensional Nanomaterials. In: Two-Dimensional Nanomaterials-Based Polymer Nanocomposites, Chapter 5 (2024) 167–194. DOI: 10.1002/9781119905110.ch5

[23]. M. Sajid, M.A. Qamar, A. Farhan, et al., Emerging Paradigms in Two-Dimensional Materials, *J. Environ. Chem. Eng*. 12 (2024) 113784. DOI: 10.1016/j.jece.2024.113784

[24]. S. Aftab, M.Z. Iqbal, S. Hussain, et al., New developments in gas sensing using various two-dimensional architectural designs, *Chem. Eng. J.* 469 (2023) 144039. DOI: 10.1016/j.cej.2023.144039

[25]. S. Li, Y. Zhang, Y. Li, et al., Modulating the photooxidation selectivity on graphitic carbon nitride, *Appl. Catal. B: Environ.* 340 (2024) 123180. DOI: 10.1016/j.apcatb.2023.123180

[26]. N. Uddin, H. Zhang, Y. Du, et al., Structural-phase catalytic redox reactions in energy and environmental applications, *Adv. Mater.* 32 (2020) 1905739. DOI: 10.1002/adma.201905739

[27]. B. Yang, A.G. Tamirat, D. Bin, et al., Regulating intercalation of layered compounds, *Adv. Funct. Mater.* 31 (2021) 2104543. DOI: 10.1002/adfm.202104543

[28]. J. Feng, X. Zhang, Y. Xu, et al., Regulating the electrolyte ion types and exposed crystal facets, *Energy Storage Mater.* 46 (2022) 278–288. DOI: 10.1016/j.ensm.2022.01.024

[29]. L. Kong, M. Zhong, W. Shuang, et al., Electrochemically active sites inside crystalline porous materials, *Chem. Soc. Rev.* 49 (2020) 2378–2407. DOI: 10.1039/C9CS00880B

[30]. H. Yang, N. Wu, Ionic conductivity and ion transport mechanisms of solid-state lithium-ion battery electrolytes, *Energy Sci. Eng.* 10 (2022) 1643–1671. DOI: 10.1002/ese3.1163

[31]. M.M. Rastegardoost, O.A. Tafreshi, Z. Saadatnia, et al., Recent advances on porous materials for triboelectric nanogenerators, *Nano Energy* 111 (2023) 108365. DOI: 10.1016/j.nanoen.2023.108365

[32]. A. Das, J. Jaiswal, R.P. Yadav, et al., Complex roughening dynamics in MoS_2 thin films, *Physica A* 624 (2023) 128989. DOI: 10.1016/j.physa.2023.128989

[33]. H. Zhu, Y. Liu, Y. Wu, et al., Electrocatalytic stability of two-dimensional materials, *J. Energy Chem.* 97 (2024) 302-320. DOI: 10.1016/j.jechem.2024.05.044

[34]. W. Dong, H. Liu, X. Liu, et al., Defective-MoS_2/rGO heterostructures with conductive 1T phase MoS_2, *Int. J. Hydrog. Energy* 46 (2021) 9360–9370. DOI: 10.1016/j.ijhydene.2020.12.087

[35]. Y. Shi, Z. Du, S. Yang. MXene–Metal Hybrids: Fabrication and Applications, *Adv. Funct. Mater.* 34 (2024) 2404653. DOI: 10.1002/adfm.202404653

[36]. S.H. Li, X.D. Sun, Y.-Z. Wang, et al., Novel mesoporous composite for NNK capture, *Chem. Eng. J.* 332 (2018) 331–339. DOI: 10.1016/j.cej.2017.09.090

[37]. L. Zu, W. Zhang, L. Qu, et al., Mesoporous materials for electrochemical energy storage, *Adv. Energy Mater.* 10 (2020) 2002152. DOI: 10.1002/aenm.202002152

[38]. S. Tamang, S. Rai, R. Bhujel, et al., Review on GO, rGO and metal oxide/rGO composites, *J. Alloys Compd*. 947 (2023) 169588. DOI: 10.1016/j.jallcom.2023.169588

[39]. I.S. Ike, I. Sigalas, S. Iyuke, Understanding performance limitation in electrochemical capacitors, *Phys. Chem. Chem. Phys.* 18 (2016) 661–680. DOI: 10.1039/C5CP05459A

[40]. Z.S. Wu, K. Parvez, X. Feng, K. Müllen, Graphene-based in-plane micro-supercapacitors, *Nat. Commun.* 4 (2013) 2487. DOI: 10.1038/ncomms3487

[41]. M. Acerce, D. Voiry, M. Chhowalla, Metallic 1T phase MoS_2 nanosheets, *Nat. Nanotechnol.* 10 (2015) 313–318. DOI: 10.1038/nnano.2015.40

[42]. Y. Tian, C. Yang, Y. Tang, et al., $Ti_3C_2T_x$//AC hybrid aqueous supercapacitors, *Chem. Eng. J.* 393 (2020) 124790. DOI: 10.1016/j.cej.2020.124790